(In)efficacy of architected auxetic materials for impact mitigation

Gärtner, T.; Dekker, Richard; van Veen, Dennis; van den Boom, Sanne J.; Amaral, Lucas

Important note
To cite this publication, please use the final published version (if applicable).
Please check the document version above.

(In)efficacy of architected auxetic materials for impact mitigation

Til Gärtner [a,b] [ID],*, Richard Dekker [b] [ID], Dennis van Veen [b], Sanne J. van den Boom [c] [ID],
Lucas Amaral [b] [ID],**

[a] *Faculty of Civil Engineering and Geosciences, Delft University of Technology, Postbus 5048, 2600 GA Delft, The Netherlands*
[b] *Unit Defense, Safety & Security, Netherlands Institute for Applied Scientific Research (TNO), Postbus 480, 2501 CL Den Haag, The Netherlands*
[c] *Unit High Tech Industry, Netherlands Institute for Applied Scientific Research (TNO), Postbus 155, 2600 CL Delft, The Netherlands*

ARTICLE INFO

ABSTRACT

It has been demonstrated that auxetic materials, characterized by a negative Poisson's ratio, offer enhanced resistance to indentation, shear forces, fracture toughness and the absorption of energy. As such, they are reported in literature to be promising options for impact mitigation in military and space contexts. Auxetic materials are rare in nature, and must therefore be designed and manufactured artificially in order to be applied. Densification of auxetic materials in order to absorb impact energy in a limited area has been the focus in the literature to date. However, this results in a concentration of the force paths, which is not desirable for impact mitigation. In this work, the effects of auxetic densification on the stress distribution over the backside of the auxetic material are addressed using both experimental and simulative trials. In this study, the distinction between auxetic and conventional honeycombs in force transmission characteristics is examined. This is achieved through an analysis of experimental data and the utilization of numerical techniques to enhance comprehension of the internal mechanisms of architected materials in response to impact.

1. Introduction

Lightweight impact protection, formerly a concern of aerospace designers due to the typical weight constraints of aircraft, has also become of interest for other applications such as vehicles, ships and infrastructure protection. Lightweight design allows for more fuel efficiency and better mobility of platforms [1], and also for using less material in infrastructure construction, contributing to sustainability goals and energy efficiency. Amongst different innovative solutions for lightweight impact protection, auxetic structures have received significant attention in recent research [2–4]. Due to the negative Poisson's ratio of auxetic materials, densification occurs when such materials are impacted, drawing material towards the impacted area, such as illustrated in Fig. 1.1. Because of this negative Poisson's ratio effect, auxetics are often considered as promising candidates to include in lightweight impact protection [2,4]. Given the absence of natural materials exhibiting negative Poisson's ratio, auxetic structures need to be architected from artificial materials to exhibit such negative Poisson's ratio for practical use. Whilst creating auxetic foams is possible [5], in impact protection literature the negative Poisson's ratio is however mostly achieved by designing auxetic lattice structures [2], such as

exemplified by the unit cell in Fig. 1.2(b). These unit cells can be repeated to create a larger lattice structure with properties resembling the unit cell. Fig. 1.2(a) shows the conventional honeycomb (CH), a non-auxetic unit cell, while Fig. 1.2(b) shows the ARH, an auxetic unit cell. The use of such auxetic lattices for impact protection reaches back decades [6], but widespread experimentation with such designs has recently become popular due to advances in manufacturing techniques such as 3D printing. Whilst experimental campaigns require significant efforts in time and money, FE modelling approaches provide a fast way to supplement the experimental findings and have been a staple in designing and improving auxetic materials in the last decades [4]. Within the FE modelling, one can speed up the computation even further by abstracting the present structure into its structural elements instead of viewing the structure as three-dimensional solids (e.g. [7–9]).

Because the beneficial properties of auxetic materials are promising in the search for lightweight impact protection, a plethora of studies on auxetic lattices used as blast and ballistic protection has been published in the past years, many of them focusing on the ARH as a simple auxetic solution [2]. Although such studies indicate the ARH almost unanimously as a better choice for impact and blast protection than
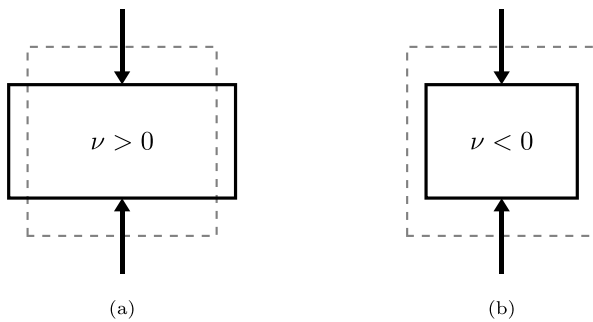

Fig. 1.1. (a) Positive Poisson's ratio materials ($\nu > 0$) and (b) negative Poisson's ratio or auxetic materials ($\nu < 0$) under compression.

conventional lattices [2,10,11], the published research fails to articulate why or how designers should incorporate such auxetic lattices in real applications, and what design parameters the designer should focus on to enable impact mitigation.

Consider, as an example, the illustration in Fig. 1.3. Materials with a positive Poisson's ratio will spread the load onto a wider area, as illustrated in Fig. 1.3(b). Negative Poisson's ratio materials (Fig. 1.3(c)) on the other hand, concentrate the load onto a smaller area. This effectively means that the distributed force results in less pressure being exerted on the protected structure. This anecdotal example aims to illustrate in simple terms that not in all cases auxetic protection systems will outperform non-auxetic conventional protection systems, contrary to what is concluded in [2].

When compared to the non-auxetic CH, the ARH has been shown to fold more easily when impacted, leading to earlier densification in the progress [11,12]. This earlier densification is related to the inwards folding of the ARH structures, generating the auxetic effect. Once the material is densified, it acts as a conventional solid material and thus generates a substantially higher stress level, contributing to energy dissipation. Available research focuses its conclusions on the higher energy dissipated by auxetic lattices [11,12], to claim the better performance in impact scenarios, but little is reported about other metrics to evaluate performance under impact and where this dissipated energy goes to. The effects of high peak reaction forces generated by the impacted ARH due to its densification, being transferred to the underlying structure, is currently not addressed in the available literature. The temporal and spatial distribution of the impact energy and the subsequent effects on the protection capabilities of different lattice structures have not been addressed in sufficient detail thus far. However, some studies have shown in the past that load spreading is essential for effective impact protection [13]. The transfer of a substantial quantity of energy over a brief time span to a restricted area, as a consequence of the densification of the distinct lattice structures, may prove detrimental to the efficacy of the protective measures in question. More specifically, Gupta and Ding [13] mention that absorbing energy is not enough, but that momentum has to be diverted from the impactor and distributed laterally. The structure underlying the protective layer is usually not designed to withstand high, localized loads and thus is dependent on the protective layer to spread out the load over both time and space. To the best knowledge of the authors, the only instance found in literature where the auxetic lattices are actually shown to transfer less force to the underlying structure than the CH is described in Bohara et al. [10]. The authors show that, under close-in blast load, the ARH deflects part of the blast overpressure load. The increased densification of the ARH, by drawing material to the blast-impacted zone, makes the core stiffer under the close-in blast area and more compliant on the edges of the panel, contributing to the deflection of the blast pressure [10].

In addition to the load transfer of single lattice structures, the design parameters for auxetic lattice structures, including the design

choices in relation to impact loads, had not been discussed in-depth until the recent publication of Gärtner et al. [9]. In this publication, it is shown that, for the effect of the auxeticity to have the greatest energy absorption, the impact should be localized and not over the complete length of the architected material. Localized impact results in the drawing of unloaded material from the sides towards the impact zone, thereby facilitating a wider degree of densification. Furthermore, the impact energy can be transported further laterally. However, only geometric non-linear elastic models without contact were used in that study, and no experimental validation was presented [9].

It is currently unclear whether auxetic lattices can be shown to outperform conventional lattices in impact protection applications in the real world, particularly in cases where energy dissipation is not the sole measure of performance. This contribution thus proposes an integrated approach to the design and evaluation of auxetic lattice structures for protection, which goes beyond mere consideration of their energy dissipation capabilities. It is important to note that the objective of this study is not to disprove the use of auxetics. Instead, it is to subject the metrics of performance applied to auxetics in impact protection, as well as the underlying physical mechanisms, to rigorous scrutiny. The aim is to provide a better foundation for the application of auxetic or conventional lattices as protective structures.

1.1. Objectives

The aim of this study is twofold:

Firstly, this study aims to use different metrics to evaluate and compare the performance under impact of both auxetic and conventional lattice structures. The use of different metrics, such as load transferred to the underlying structure and the distribution of the pressure at the back-face of the protective structure can give new insights in the mechanisms of impact protection of different lattices, enabling the guided design of lattice structures for impact mitigation in relation to different loading scenarios.

Secondly, in order to produce guidelines for load localization for impact protection design, the present study aims to test the hypothesis of [9], which states that in order for auxeticity to have more effect and a better impact protection, it is crucial, that the impact is localized and does not cover the complete auxetic lattice surface area.

To complete the overview of the design and analysis process of auxetic lattices, the present study combines experiments and non-linear numerical models. Furthermore, this study offers an insight into the numerical assessment methods available for architected lattices used for impact protection, by showcasing investigations possible with both detailed, continuum-based and efficient, beam-based numerical models. The continuum-based numerical model is employed to gain a deeper insight into the details of the inner deformation and load transmission processes of the experimental campaign. To supplement these investigations, the beam-based numerical model is chosen due to its efficiency to enable fast explorations into different scenarios.

1.2. Organization

The lattice structures analysed are presented in Section 2. The different physical and numerical settings employed to assess the performance of different lattice architectures in a protection lay-up are explained in Section 3. Subsequently, the results of the different analyses will be laid out in Section 4, and the advantages and limitations of each analysis will be discussed. A comparison between the different methods will be done in Section 5, as well as a discussion on the efficacy of auxeticity in protective systems and the metrics useful in entertaining this assessment and suggestions for further research.
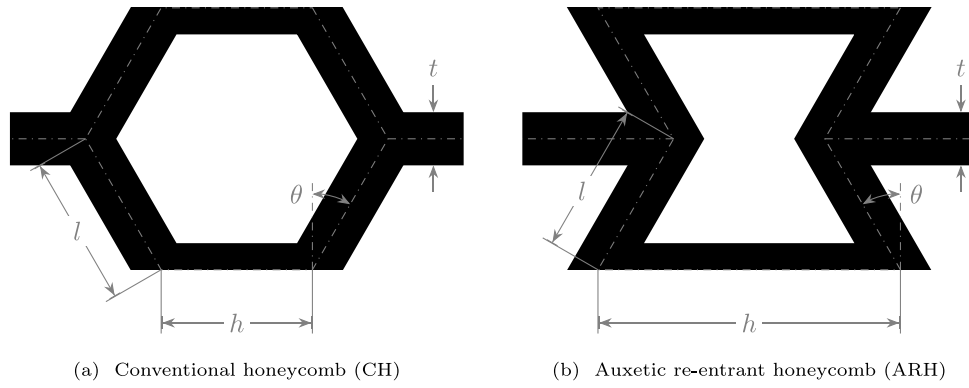
(a) Conventional honeycomb (CH)

(b) Auxetic re-entrant honeycomb (ARH)

Fig. 1.2. Comparison of (a) conventional and (b) auxetic re-entrant honeycomb lattice structures.
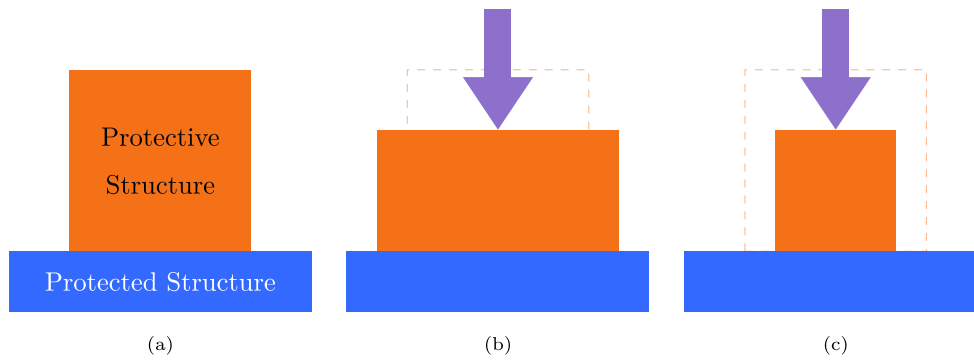

(a)

(b)

(c)

Fig. 1.3. Illustration of an example where auxetic lattices might be detrimental to the structure to be protected. (a) Unloaded structure; (b) structure with positive Poisson's ratio under load; (c) structure with a negative Poisson's ratio under load. Contact area is larger for structure with positive Poisson's ratio, transferring smaller stresses to underlying structure. Dashed lines represent the shape of the undeformed structure.
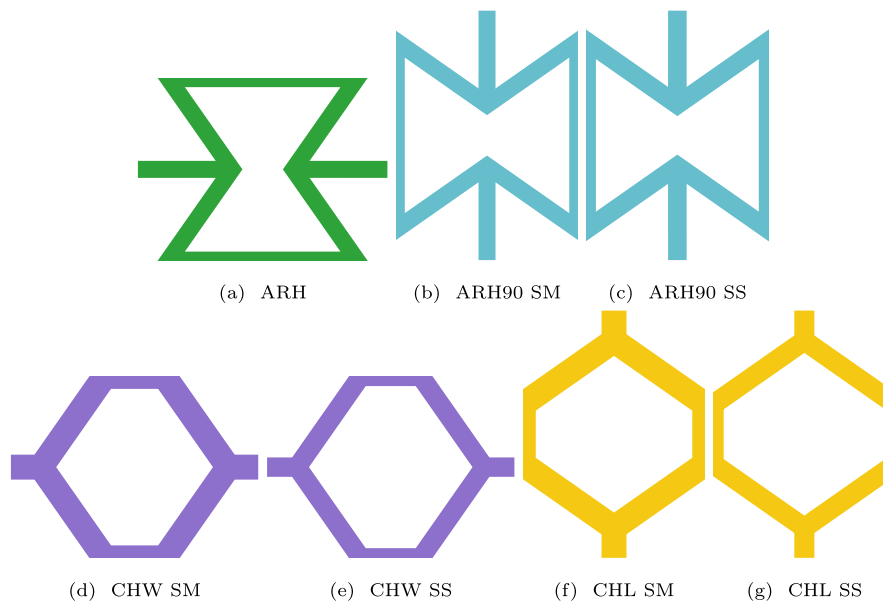

(a) ARH

(b) ARH90 SM

(c) ARH90 SS

(d) CHW SM

(e) CHW SS

(f) CHL SM

(g) CHL SS

Fig. 2.1. Unit cells.

Table 2.1

Dimensions, mass and initial elastic stiffness along impact direction of the unit cells considered in the present study (see Fig. 1.2 for the definitions of the dimensions).

	Unit cell	*l* (mm)	*h* (mm)	*θ* (°)	*t* (mm)	Mass (g)	Stiffness (GPa)
SS	ARH	4.8831	8.30	35	0.750	5.50	2.49
	ARH90	4.8831	8.30	35	0.820	5.98	2.49
	CHW	4.8831	2.65	35	0.854	3.99	2.48
	CHL	4.8831	2.65	35	0.884	4.12	2.49
SM	ARH90	4.8831	8.30	35	0.750	5.50	1.91
	CHW	4.8831	2.65	35	1.100	5.04	5.2
	CHL	4.8831	2.65	35	1.100	5.04	4.71

Table 2.2

Dimensonless properties of the unit cells considered in the present study.

	Unit cell	rel. density (%)	rel. stiffness (%)	max. slenderness	Poisson's ratio
SS	ARH	31.25	1.19	11.1	−0.95
	ARH90	33.98	1.19	10.1	−0.77
	CHW	22.67	1.18	5.7	0.95
	CHL	23.41	1.19	5.5	0.86
SM	ARH90	31.25	0.91	11.1	−0.80
	CHW	28.64	2.48	4.4	0.89
	CHL	28.64	2.24	4.4	0.82

2. Investigated architectures

This study investigates architected materials, as shown in Fig. 1.2, where Fig. 1.2(b) shows the auxetic re-entrant honeycomb (ARH), an auxetic lattice, while Fig. 1.2(a) shows a conventional honeycomb (CH), a non-auxetic lattice. The ARH has been chosen as the baseline auxetic lattice for comparison. This choice is based on its widespread use in literature (e.g., [2,10–12]), and the dimensions of the baseline ARH are described in Table 2.1 together with the estimated mass and stiffness of one unit cell. The initial elastic stiffness of the samples in Fig. 2.1 was estimated using linear elastic, small deformation FE analyses considering an elastic modulus of 210 GPa and a Poisson's ratio of 0.265, corresponding to the steel grade used to manufacture the samples. Linear elastic FE analyses were conducted instead of analytical models (such as the one from Gibson et al. [14]) to estimate the initial elastic stiffnesses of the samples due to the relatively thick struts of the lattice structures. In addition, the impact protection performance of the ARH is compared to the same structure rotated by 90°, in the following called auxetic re-entrant honeycomb (90° rotated) (ARH90). In order to shed light on the effects of auxeticity in comparable circumstances, the non-auxetic unit cells conventional honeycomb (W-configuration) (CHW) and conventional honeycomb (L-configuration) (CHL) are investigated as well. The dimensions of the struts of the ARH90, CHW, and CHL samples were selected to guarantee that a set of such samples with the SM as the ARH is obtained. Additionally, another set of unit cells with the SS as the ARH in the impact direction is designed and evaluated throughout the study. The unit cells of each investigated lattice are illustrated in Fig. 2.1, while the unit cell masses, dimensions and initial elastic stiffnesses are described in Table 2.1. In order to give a better estimation for the overall behaviour of the unit cells, the relative density and relative stiffness related to the base material are reported in Table 2.2. In this table, also the maximum slenderness, i.e. the length of the longest beam divide by the thickness of the beams is reported. It can be seen, that the re-entrant types are more slender, and thus more prone to buckling. The vertical Poisson's ratio relates the horizontal compression or extension with the compression in impact direction and is reported in Table 2.2 as well. It should be noted here, that the Poisson's ratios greater than 0.5 reported for the honeycomb unit cells do not violate any bounds on the Poisson's ratio given the orthotropic nature of these metamaterials.

In addition to the initial elastic stiffness, quasi-static stress–strain curves were extracted for the investigated unit cells. These investigations were done using fully nonlinear FE analyses using planar
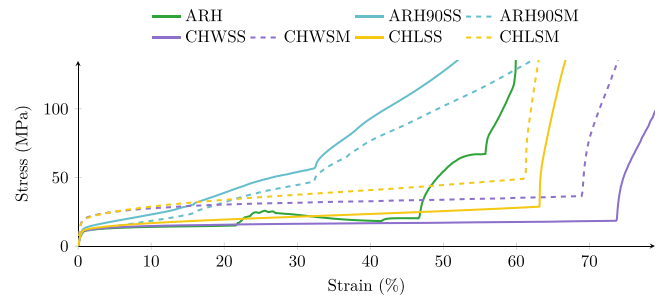

Fig. 2.2. Static compression response of single unit cells.

Table 2.3

Measured or estimated mass of the auxetic samples which are shown in Fig. 2.3. The samples of *Length 1* were not measured with a digital scale but, instead, the mass was estimated via CAD model assuming a density of 8000 kg m⁻³.

	Unit cell	Length 1			Length 2		
		n_x	n_y	Mass (g)	n_x	n_y	Mass (g)
SM	ARH	6	8	733.08	12	8	976.75
	ARH90	8	6	733.15	16	6	977.05
	CHW	6	8	732.61	12	8	970.15
	CHL	8	6	732.75	16	6	971.21
SS	ARH90	8	6	742.35	16	6	1023.05
	CHW	6	8	669.46	12	8	872.96
	CHL	8	6	688.43	16	6	884.48

boundary conditions, that ensure all edges remain plane but are free to move. The resulting curves are shown in Fig. 2.2 up to the point of full densification. The onset of plasticity after around 1% compression is clearly visible in all architectures. Within the elastic range of deformation, the differences in initial stiffness between the architectures are emphasized, particularly the substantially increased stiffness of the CH architectures of similar mass. This results in a higher stress at the yield point and subsequently higher stresses throughout the plateau stage. Comparing the SS and SM variants of all unit cells, the higher initial stiffness reported in Table 2.1 also correlates with a higher energy absorption potential in all cases. It should be noted as well, that buckling of the load-carrying beams at the lateral edges of the ARH90 and CHL unit cells is prevented by the planar boundary conditions. This results in an overestimation of the stresses for these particular unit cells. The effects of self-contact can distinctly be seen in all architectures up to the point of total densification. The auxetic structures densify earlier due to their convex nature. As densification leads to direct force transmission through the sample, the longer plateau phase of the CH architectures is beneficial in practical applications if sufficient to absorb the impactor's energy before densification.

2.1. Sample configuration

The previously described unit cells are assembled into lattice structures with two sizes of the entire patch: One size, in the following denoted as *Length 1*, has approximate measures of 65 mm × 65 mm. A sample twice as wide and denoted as *Length 2*, measures approximately 130 mm × 65 mm. To achieve these measures multiple units cells were stacked both vertically and horizontally, with a base of solid steel, 10 mm high, and a strike face on the upper side being 65 mm wide and likewise 10 mm high. The physical samples produced for the ARH architecture are shown in Fig. 2.3 for both lengths investigated. An overview over the number of unit cells in each direction and the resulting mass for the samples is given in Table 2.3. These patches with a depth of 25 mm are investigated for all further experimental and numerical studies unless otherwise noted.
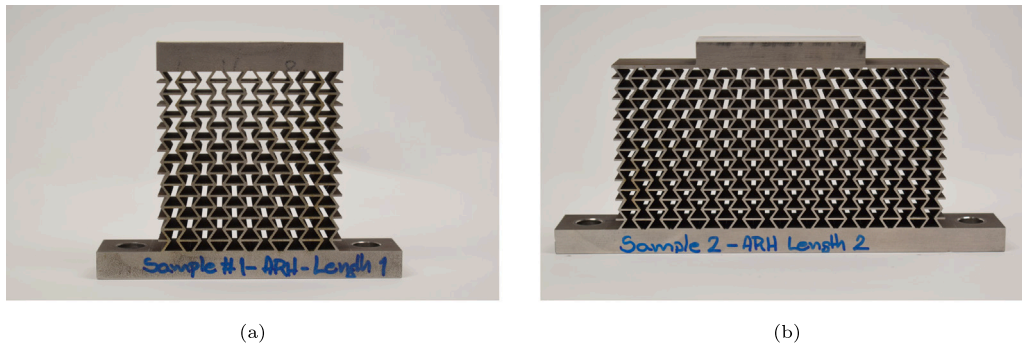
(a)

(b)

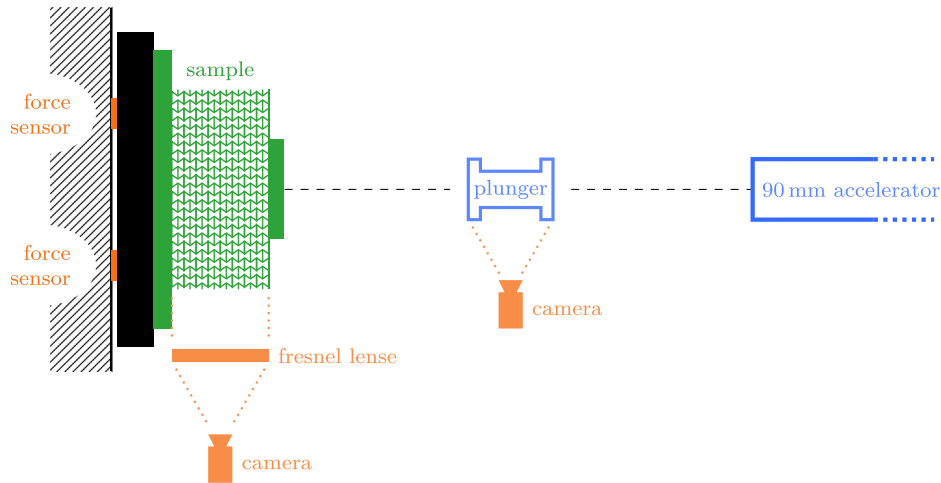**Fig. 2.3.** Assembly of ARH unit cells into patches to be investigated, (a) *Length 1* and (b) *Length 2*.

Fig. 3.1. Schematic view of the experimental set-up.

Table 2.4
Physical & numerical investigation matrix.

	Unit cell	Length 1	Length 2
SM	ARH	Physical/numerical	Physical/numerical
	ARH90	Only numerical	Physical/numerical
	CHW	Only numerical	Physical/numerical
	CHL	Only numerical	Physical/numerical
SS	ARH90	Only numerical	Physical/numerical
	CHW	Only numerical	Physical/numerical
	CHL	Only numerical	Physical/numerical

2.2. Test matrix

In order to assess the effects of the different lattice architectures as well as the effect of localization of an impact, as was suggested by [9], all architectures are tested according to the test matrix shown in Table 2.4. The effect of impact localization is experimentally carried out only for the ARH as baseline architecture. For the assessment of the other lattice architectures additional FE analyses are conducted.

3. Methods

3.1. Experimental set-up

3.1.1. Sample manufacturing

The samples, with geometries as described in the previous section, have been manufactured by electric discharge machining (EDM). EDM was chosen for its tight geometric tolerances, which are required to ensure that the radii in the corners of the structures are sufficiently small to ensure that the physical samples resemble the desired structures. EDM is an inherently precise method, with the accuracy only limited by the size of the electrode, and maintains this accuracy for relatively large material depths.

A good material for lattice samples in impact condition will have a high yield strength and stiffness, in combination with being very ductile. These properties ensure sufficient energy can be dissipated during the deformation. The only condition that EDM poses on the material is that it conducts electricity, rendering metals a prime choice. After careful evaluation 316 stainless steel (AISI 316L) was chosen for producing the sample set later used in the experimental campaign. This was motivated mainly by the high strain to failure (>25%), ensuring the structure folding neatly without hinges breaking and losing structural integrity. This high toughness additionally absorbs a significant amount of energy in the process.

3.1.2. Testing set-up

For the test series, the lattice samples manufactured by EDM were attached to a 30 mm thick steel base using four M10 bolts. A construction drawing of this set-up can be found in Fig. 3.2. The base was then attached to a stiff boundary using four M16 bolts and 4 Piezoelectric ring force transducers from the brand Kistler, type 9104C. The Kistler ring force transducers have a load limit of 160 kN and an axial stiffness of 7.5 kN μm^{-1} per transducer. All lattice samples were impacted by a plunger with a mass of 1.2 kg and made of aluminium. The experimental set-up is shown in Fig. 3.3, while drawings of the plunger are shown in Appendix A. All tests are carried out with a nominal impact velocity of 70 m s^{-1}. The experimental procedure was recorded digitally by two high-speed cameras at 25 000 fps, one directed at the lattice to capture its performance, and the other at the plunger mid-flight to
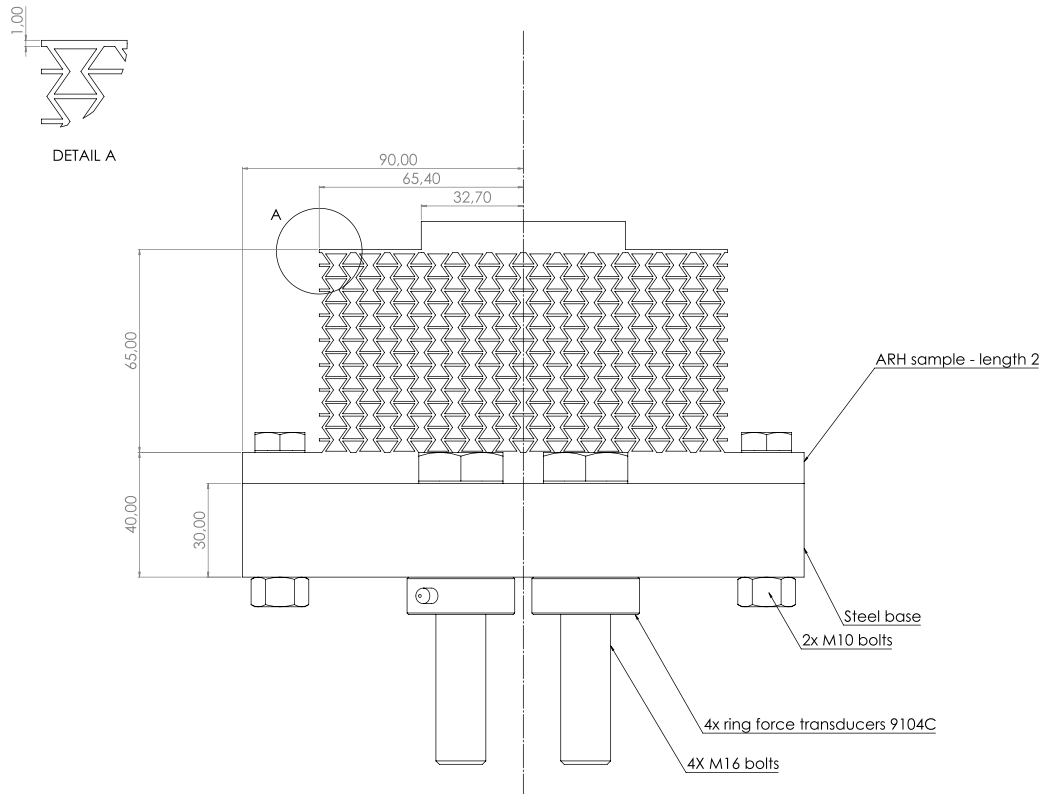
Fig. 3.2. Side view of the sample mounting in the experimental set-up with main dimensions and components - dimensions in mm.

(a) Position of the camera with Fresnel (b) Shooting barrel and camera pointing at the sample.
lens.

Fig. 3.3. Experimental set-up.

assess the projectile orientation and velocity. A schematic overview over the entire set-up can be found in Fig. 3.1.

3.2. Continuum-based FE

Explicit non-linear FE analyses were performed using the commercial software package ABAQUS. An example of a simulated assembly is given in Fig. 3.4, which consists out of the lattice specimen and the plunger impacting the specimen. The specimen is fully fixed at its support and the 1.2 kg weighing plunger is given an initial vertical velocity, matching that of the experiments. The plunger was modelled in a simplified manner, as a rectangle of 20 mm height and 65.4 mm width (compare Fig. 3.4). Note that, in order to maintain the mass of the plunger the density of this block was adjusted to 36 703 kg m^{-3}. All contact interactions were modelled by hard normal contact and frictionless tangential behaviour. The simulation were performed in 2D,

assuming plane strain, where the depth of the specimen and the plunger were set to 25 mm. Four-node quadrilateral elements with reduced integration (type CPE4R), having an average element size of 0.12 mm, were used. This resulted for the ARH sample of *Length 2* in 192 520 elements and 438 206 degrees of freedom (DOFs). A close-up of the mesh showing two unit cells is given in Fig. 3.5. As indicated earlier, the lattice is made out of stainless steel and the plunger out of aluminium. Both materials were simulated using a Johnson-Cook plasticity model to account for strain rate effects [15]. In this model, the von Mises yield surface is described by

$$\bar{\sigma} = \left[A + B \left(\bar{\varepsilon}^{\text{pl}} \right)^n \right] \left[1 + C \ln \left(\frac{\dot{\bar{\varepsilon}}^{\text{pl}}}{\dot{\bar{\varepsilon}}_0} \right) \right], \quad (3.1)$$

with the equivalent plastic strain $\bar{\varepsilon}^{\text{pl}}$, the equivalent reference strain rate $\dot{\bar{\varepsilon}}_0$ and the numerical parameters A, B, C, n. These properties and parameters used for both materials, following from literature [16,17], are given in Table 3.1.

Table 3.1

Material properties and parameters for the FE simulation.

Material	E [GPa]	v [−]	A [MPa]	B [MPa]	C [−]	n [−]	$\dot{\epsilon}_0$ [−]	ρ [kg m^{-3}]
Stainless steel [17]	210	0.265	280	1750	0.1	0.8	0.02	8000
Aluminium [16]	72	0.33	103	350	0.12	0.4	0.001	36 703[a]

[a] Note that the density of aluminium is chosen such that the plunger mass is equal to 1.2 kg and is therefore not equal to the real density of aluminium.
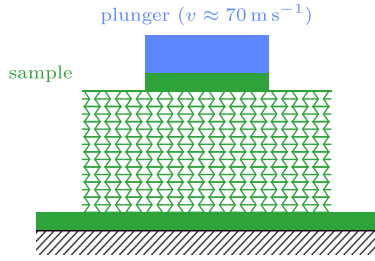
Fig. 3.4. Geometry, boundary conditions and initial conditions for the FE analyses.
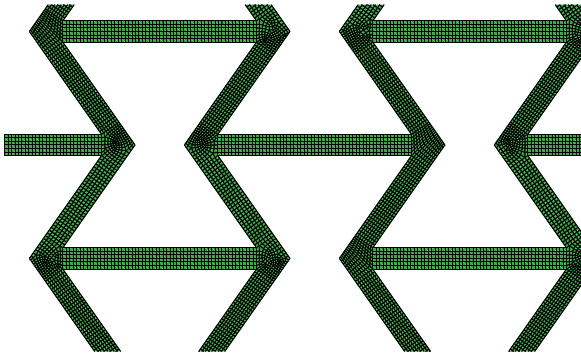
Fig. 3.5. Close-up of the mesh for two unit cells.
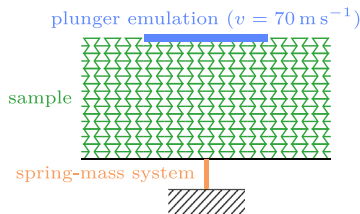
Fig. 3.6. Geometry and boundary conditions for the JIVE analyses.

3.3. Beam-based FE

The structures investigated can be viewed as a collection of beams into a lattice. In order to accelerate and simplify the simulations described in Section 3.2, and to allow for a faster processing of different configurations, these lattice structures are also implemented as a collection of Simo-Reissner beams (after [18,19]). The FE implementation in the JIVE-framework [20] follows [21] with the corrections proposed by [22]. This results for the ARH sample of *Length 2* in 16 824 DOFs, which is a reduction by more than one order of magnitude compared to the continuum-based model in Section 3.2.

The material of the structure is modelled as elasto-plastic beams with kinematic hardening (cf. [23]). For the elastic behaviour a Young's modulus of 210 GPa and a Poisson's ratio of 0.265 are assumed in accordance with the assumptions in the solid model. The beams are modelled as square beams with a side length of 0.75 mm and the shear

correction coefficient is set to 5/6. The yield function

$$
\Phi = \left| \frac{N_1}{71.8\,\text{N} - N_1^h} \right|^{2.68} + \left| \frac{N_3}{164\,\text{N} - N_3^h} \right|^{1.75} \\
+ \left| \frac{M_2}{30.8\,\text{N mm} - M_2^h} \right|^{1.93} - 1,
$$

(3.2)

with the stress resultants N_1 for the shear force, N_3 for the axial force, M_2 for the bending moment, and the corresponding hardening contributions N_1^h, N_3^h, M_2^h, is accompanied by the kinematic hardening tensor

$$
H = \begin{bmatrix} 936\,\text{N} & 1630\,\text{N} & 618\,\text{N mm} \\ & 2800\,\text{N} & 907\,\text{N mm} \\ \text{sym.} & & 443\,\text{N mm}^2 \end{bmatrix}.
$$

Further details on the elasto-plastic beam formulation and their scaling for different beam sizes can be found in [23,24] and are not part of this contribution.

For an adequate model of the beam connections slight modifications to the beam geometry have been applied. In accordance with [8], the last elements in each beam are assumed purely elastic and thickened by a factor of 1.25 for the stiffness calculation and thinned by a factor of 0.75 for the inertia calculation. Contact is implemented with friction-less sliding for linear two-node elements, following [25] for node-to-element contact. In the present two-dimensional set-up, only node-to-element contact is occurring, and the penalty parameter is set to 4×10^6. For dynamic simulations a predictor–corrector approach with automatic step-size control using a Milne-device is employed.

The set-up for the beam-based FE analyses is shown in Fig. 3.6. Notable differences to the solid-based analyses in Section 3.2 are the emulation of the impactor at the upper side by adding a virtual mass totalling 1.2 kg to the nodes on the impact surface, as well as the replacement of the lower plate by a "beam" acting as a spring-mass system emulating the baseplate.

4. Results

To ensure the comparability of the different models, they were in a first step compared to each other. For this comparison ARH samples of both lengths were used. The total force recorded at the back face is shown over the time for all three models in Fig. 4.1. One should note here, that the stopping points for all models are different, the experiment stops as soon as the total recorded force reaches 0 N, the continuum bases simulations are run for 1.3 ms and the beam-based simulations are run until the plunger velocity reaches 0 m s^{-1}.

When comparing the force recordings, an overestimation of the forces in the FE models can be observed. Such overestimation can be explained by the fact, that in the experiment the backing is not infinitely stiff, whereas the simulations assume a fully rigid boundary condition. In the high-speed videos a flexing motion of the backplate is observed, despite the best efforts to obtain a stiff test set-up. This effect of overestimating the force levels is also seen for all other simulations of the experimental cases described in Table 4.1. The comparisons for other architectures are shown in Appendix B. In general all simulations show higher force levels as well as a higher initial peak. Both of these phenomena can be explained by the rigid backing assumed in the simulation.
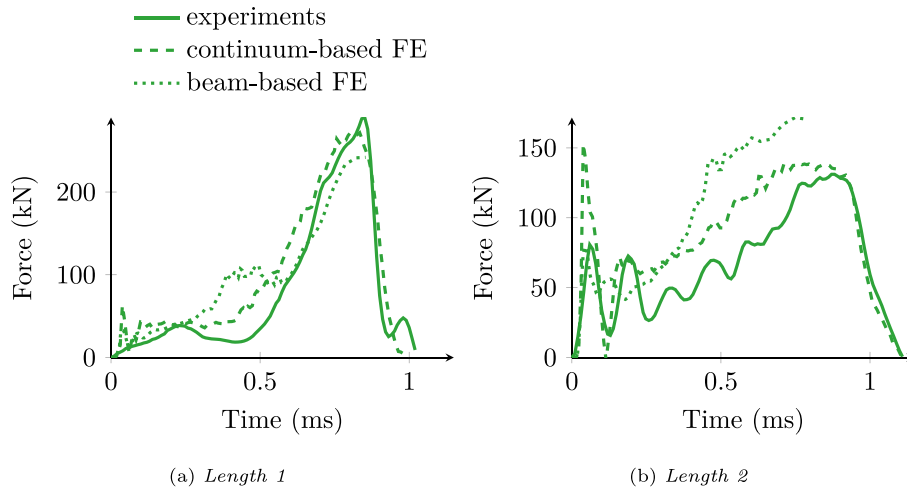
Fig. 4.1. Comparison of the three models from Section 3 for ARH samples of (a) *Length 1* and (b) *Length 2*.
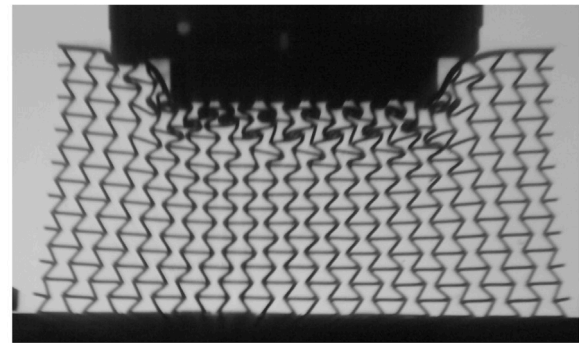
As the over-prediction of the force is a phenomenon observed in the correlation of all simulations with their respective experimental cases and not severe, the simulations were deemed trustworthy for the assessment of differences in the behaviour of different architectures. However, it was decided to exclude the first 0.15 ms from the computation of integral measures, such as the average or maximum pressure, in order to exclude the effects of the higher initial peak.

Further illustration for all models is provided in Fig. 4.2. In this figure, the *Length 2* ARH sample is shown in all three investigation settings after 0.25 ms. Here, it is observable, that both FE models show a stronger indentation of the plunger compared to the experimental model, which is again explained by the higher forces due to the rigid backing. Other than that, despite not matching the deformation of each singular member in the lattice precisely, the overall deformation pattern between the experiments and the FE models match closely. Especially the start of the densification in the upper end of the sample as well as stronger densification around the edges of the strike-face are matched well. This confirms the assessment based on the total force recordings, that the models are comparable and valuable insights can be gained by exploring all three models available.

4.1. Experiments

The first set of experiments were conducted on the baseline ARH for both patch configurations, *Length 1* and *Length 2*. Both samples are displayed in an undeformed state in Fig. 2.3. The corresponding recorded forces on the back-face are shown in Fig. 4.3 over time measured from the initial contact between the plunger and the front face of the sample. In this figure it is observed that the initial part of the load is lower and more stable for the globally impacted sample of length 1. However, a large peak in the measured reaction force occurs after 0.8 s, followed by a subsequent sharp drop to 0 N. In contrast, the sample of *Length 2* exhibits a more dispersed impact load (and, consequently, impact energy) over time, maintaining a relatively constant transmitted force until the plunger is fully stopped. This comparison indicates that the surrounding material is crucial for the determination of the protection level of a structure. From the level of force, a localized impact is to be preferred in order to spread out the momentum transfer over a longer time resulting in a lower peak force throughout the time.
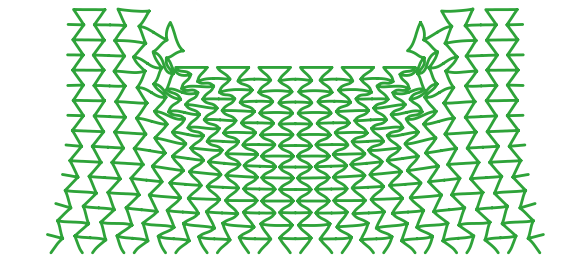
Subsequent experiments were conducted to compare other auxetic and non-auxetic architectures, as specified in Table 2.3, with the baseline ARH sample described above. The actual impact velocity and masses of each plunger were measured and are described in Table 4.1. In the first series, all four samples were designed to have the same initial elastic stiffness. Fig. 4.4(a) shows the force summed up over the
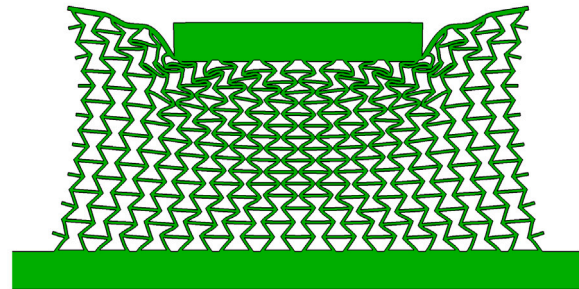
Fig. 4.2. Comparison of the deformation of the *Length 2* ARH sample at 0.25 ms. (a) is showing the experimental image, (b) the continuum-based FE result, and (c) the beam-based FE result.
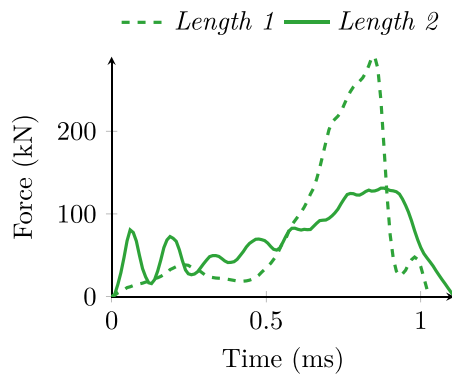
Fig. 4.3. Experimental comparison of samples sizes for ARH.

Table 4.1
Recorded plunger velocities and masses.

	Unit cell		Velocity (m s^{-1})	Mass (g)
	ARH	Length 1	74	1202
	ARH	Length 2	71	1199
SS	ARH90	Length 2	76	1202
	CHW	Length 2	75	1199
	CHL	Length 2	75	1202
	ARH90	Length 2	72	1200
SM	CHW	Length 2	77	1199
	CHL	Length 2	73	1192

sensors plotted over time. Note that the force measurements due to the rebound of the plunger are not shown here as they are not the focus of this research. Both auxetic structures—ARH and ARH90SS—show a distinct peak in the force curve. Upon examination of the high-speed videos, it can be observed that this correlates with the point at which the material is approaching complete densification. Consequently, the subsequent deceleration of the plunger is solely due to material compression, requiring significantly greater forces compared to the lattice deformation in the earlier stages of the impact. Stills from the high speeds videos of both—ARH and ARH90SS—can be found in Fig. 4.5. In contrast, the conventional honeycombs in both orientations do not show a distinct peak, but rather a slower deceleration at lower forces. Here, due to the positive Poisson's ratio of the material, the structural members of the lattice are laterally pushed away from the impact location. This effect spreads the load over a larger area, as the laterally pushed away material deforms as well. This lateral deformation can be observed in Fig. 4.6, where stills of the high speed videos throughout the deformation are shown for both CHSS configurations. The details of this spatial load distribution were investigated further in the numerical experiments.

Another comparison is undertaken with the lattices designed to exhibit a similar mass as the ARH baseline architecture. The corresponding measured forces over time are shown in Fig. 4.4(b). The ARH curve is the same as in Fig. 4.4(a), as this architecture is used as baseline. The rotated auxetic structure (ARH90) possesses a less distinct, more flat peak. The CH curves are higher than Fig. 4.4(a) curves, due to the higher stiffness resulting from the thicker beams due to the equivalent mass design target. These higher initial stiffnesses are recorded Table 2.1. Both conventional honeycombs show the same peak-less behaviour as described for Fig. 4.4(a), but at a higher level.

4.2. Continuum-based FE

In order to enhance understanding of the physical experiments, numerical simulations were conducted as detailed in Section 3.2. Simulations allow the extraction of data from any point, without any physical restrictions and effects on the results. Of special interest in the

context of impact mitigation is not only the total force transmitted to the back of the protective structure, but also the pressure distribution over the back face. For this the average and maximum pressure onto locations of the back-face were computed over time, with the exclusion of the first 0.15 ms as described above. The average pressure over the back-face is shown in Fig. 4.7(b) for all architectures with the same stiffness. This average pressure distribution in Fig. 4.7(b) shows that the auxetic densification leads to a concentration of the forces on a smaller area, resulting in a higher pressure onto the protected structure at the back of the plate. It should be mentioned that the highest average pressures for the non-auxetic structures are at the edges of the lattice structure, indicating, that the length of the CH samples is not sufficient to spread the load effectively. This is emphasized by the observation of similar pressure distributions in the samples with only the single width, as shown in Fig. 4.7(a). Here the auxetic samples concentrate the force in the centre, resulting in higher pressures onto the backside, whereas the non-auxetic samples distribute force to the boundaries. A point to note here is that the CHL architecture also shows a slight peak in the centre of the structure. This can be explained by the deformation of this unit cell leading to auxetic behaviour, as shown previously [9].

Similar observations can be made upon examination of the maximum pressure on the backside. For the *Length 2* samples, this is shown in Fig. 4.8(b) and for the *Length 1* samples in Fig. 4.8(a). The load spreading effect is less distinct, but still observable in the plot showcasing the *Length 2* samples. In the plot with the *Length 1* samples the discussed effects of CHL architectures becoming auxetic is even more prevalent. This is also observable in the deformation throughout the physical experimentation in Fig. 4.6. Similar behaviour can be seen in Appendix C for the SM configuration.

4.3. Beam-based FE

Using the more efficient beam-based model, investigations into wider samples are available for fast computation. For this, all SS samples reported in Table 2.1 as *Length 2* are elongated in the horizontal direction again, leading to a doubling of the unit cells in *x*-direction, whilst all other boundary conditions are kept the same. In Fig. 4.9, again, the recorded total force on the back-face is shown over time. The solid lines represent the samples of *Length 2*, whereas the samples of *Length 4* are shown in dashed lines. No substantial difference between the two sample widths can be observed, indicating together with the results from the continuum-based simulation, that the increase in length does not affect the total force transmission profile, but only the pressure distribution. The same accordance between the configurations can be found when examining the results for the SM configurations in Appendix C

Another additional study enabled by the structural FE modelling is the change of the unit cell size. For this, unit cell sizes are halved and the number of unit cells reported in Table 2.1 in each direction is doubled in order to have the same outer measures for each sample. This leads to a quadrupling of the overall number of unit cells whilst keeping the mass the same. In Fig. 4.10 the comparison between the two investigated sizes is plotted for the samples of *Length 1* in the SS configuration. In this graph, the force on the back-face is shown for all different unit cells over the time. The default unit cells of *Size 1* are shown in solid lines, whereas the adapted unit cells of *Size 0.5* are depicted with dashed lines. In the graph it can be observed, that reducing the size of the unit cells does not lead to any significant change in the transmitted forces. The same effect is also seen in the *Length 2* samples, as well as in the SM configuration samples, which can be found in Appendix C.

In order to appreciate the effect of velocity additional studies at different velocities were carried out. In these investigations, the mass of the impactor was kept the same, but the speed was adapted, so that the kinetic energy or the impulse of the impactor were doubled and halved, respectively. For a doubling of kinetic energy, the velocity
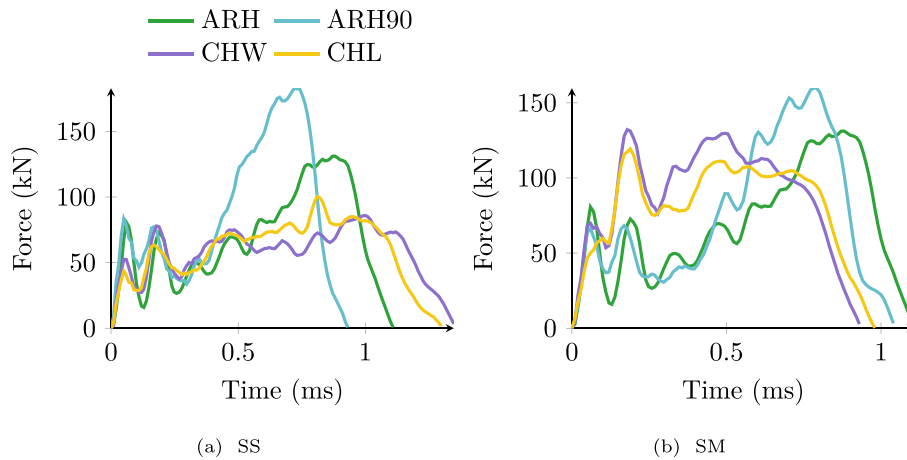
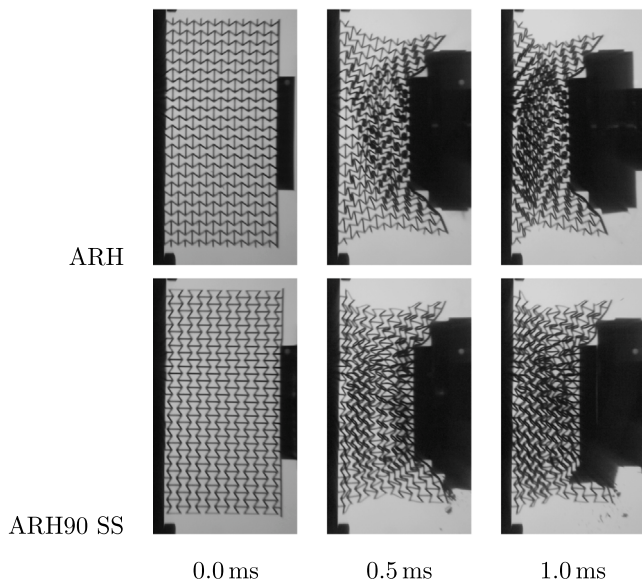**Fig. 4.4.** Force comparison for same (a) stiffness and (b) mass from the physical tests.

Fig. 4.5. Stills from the high-speed recordings for both auxetic architectures.
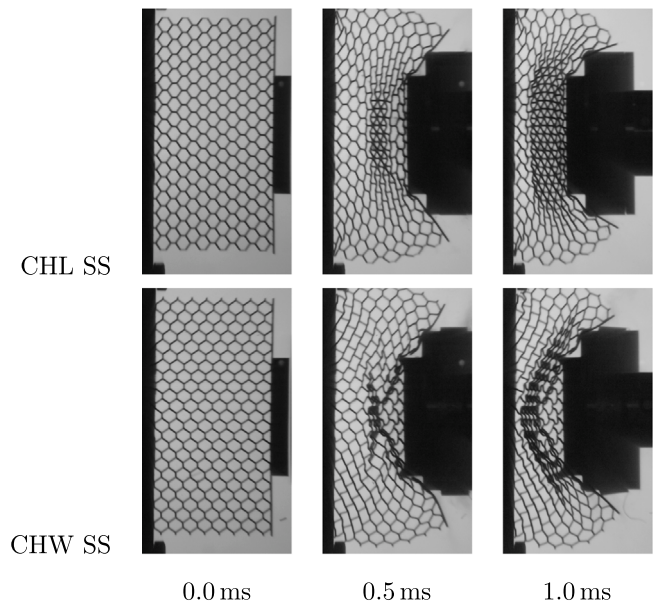

Fig. 4.6. Stills from the high-speed recordings for both non-auxetic architectures.

of the impactor needs to be multiplied by $\sqrt{2}$, and for halving it divided by $\sqrt{2}$ likewise. This resulted in the list of 35 m/s, 49.5 m/s, 70 m/s, 99.0 m/s and 140 m/s as investigated speeds, including the original study. In Fig. 4.11, the ARH architecture is showcased for all 5 investigated speeds and at 5%, 10%, 15%, 20% and 25% compression each. One should note, that the visualizations at the same compression level do not correspond to the same time, as the compression occurs faster at higher impactor velocities. In the central row, the speed discussed in the previous parts of this study is shown. The deformation pattern emerging at this speed showcases a *V*-shaped manner, similar to the transitional mode discussed in [26]. As reported in literature, for higher velocities a transition and concentration of the dynamic collapse zone towards the strike face can be observed. For lower velocities, we observe the emergence of the collapse pattern from the bottom of the patch. When inspecting the lateral contraction, the Poisson effect appears to be weakening with increased impact velocities. At the target velocity for this study of $70 \, \text{m s}^{-1}$, the lateral contraction is still clearly visible throughout the sample, indicating the applicability of this speed for studying the effects of the Poisson effect. This can also be seen in Fig. 4.12, where at lower speeds the effect of the negative Poisson's ratio is showcased by material being pulled towards the centre, whereas for higher speeds, the effect is subdued by the inertia of the material.

Similar effects can be observed for the other investigated materials as well, they are shown in Appendix D.

5. Discussion & conclusion

Looking back at the experimental campaign that resulted in the transmitted force onto the underlying material after a localized impact, it is first observed, that higher stiffness leads to more direct force transmission. Whilst all samples are able to absorb the impact energy, this showcases CH structures outperforming ARH structures when the main concern is energy absorption in a limited area with a given weight, as they were able to do so in a shorter time. Reducing this stiffness allows the energy absorption to be spread out over a longer time for the CH samples, that are not stiffening unlike the ARH samples. This spread of the energy absorption results in lower total force levels on the back-face of the protective structure, potentially reducing the load on the precious load being protected by the lattice, which is beneficial for the protection as reported by Gupta and Ding [13]. While under blast loading, the more compliant edges can help distribute the force, as reported by [10], due to the external load spread inherent to a blast. Under ballistic impact, the load is naturally concentrated and
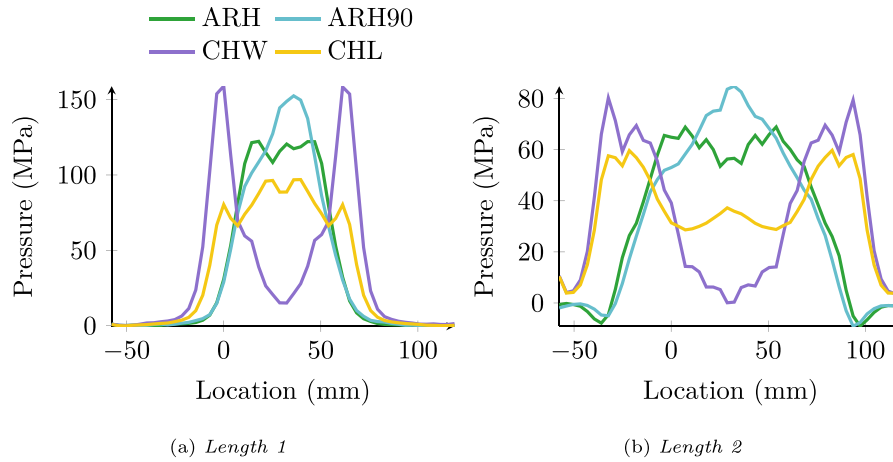
Fig. 4.7. Comparison of the average pressure over the back-face for the SS configuration using the continuum-based model.
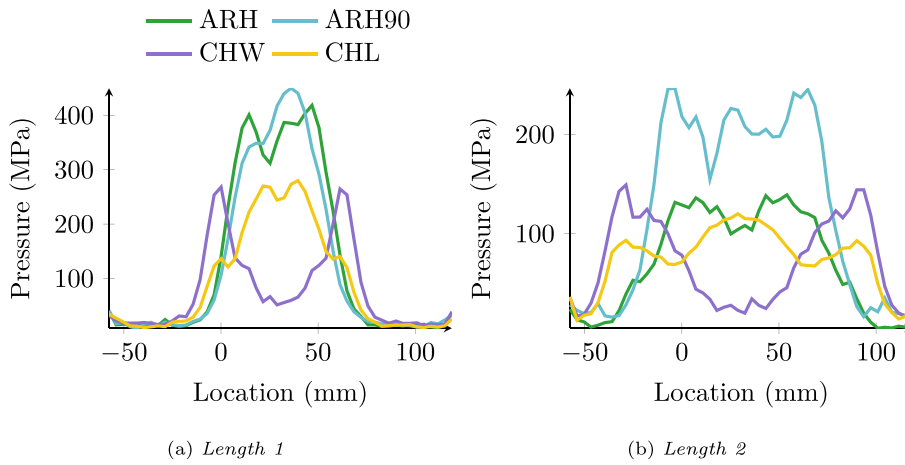

Fig. 4.8. Comparison of the maximum pressure over the back-face for the SS configuration using the continuum-based model.
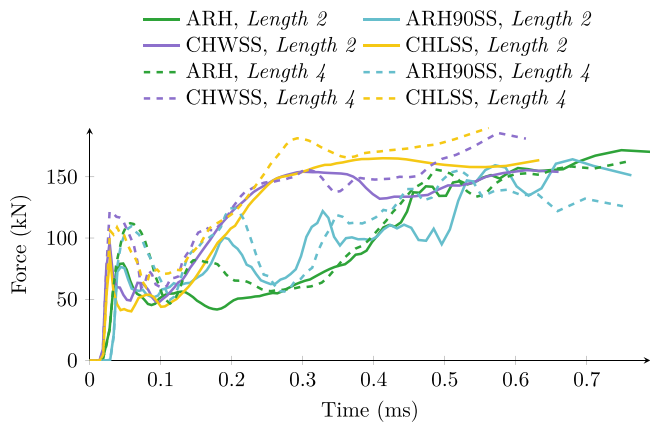

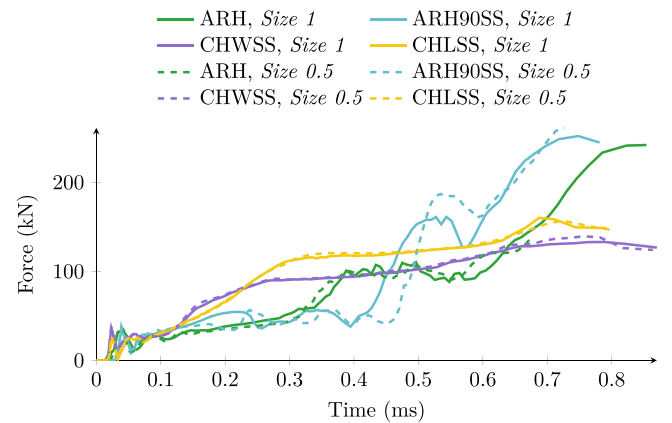**Fig. 4.9.** Comparison of longer samples for the SS configuration.

Fig. 4.10. Comparison of smaller unit cells for the SS configuration of *Length 1* using the beam-based model.

thus negative Poisson's ratio and the corresponding densification and stiffening lead to a further concentration of the load.

These finding are reinforced by the additional numeric studies into the load spread on the back-face of the material. Here, it can be summarized, that in the given context, a negative Poisson's ratio in the material leads to higher peaks in the loading on the backside of the protective structure also in space. This effect is especially pronounced when comparing the structures with comparable stiffness.

When looking at structures with equivalent mass, the higher stiffness of the conventional architectures has a stronger effect compared to its load distribution effect. Overall it has been shown, that higher stiffness improves the energy absorption qualities in a confined space, but also lead to worse protective properties due to higher force peaks onto the back-face of the protective structure.
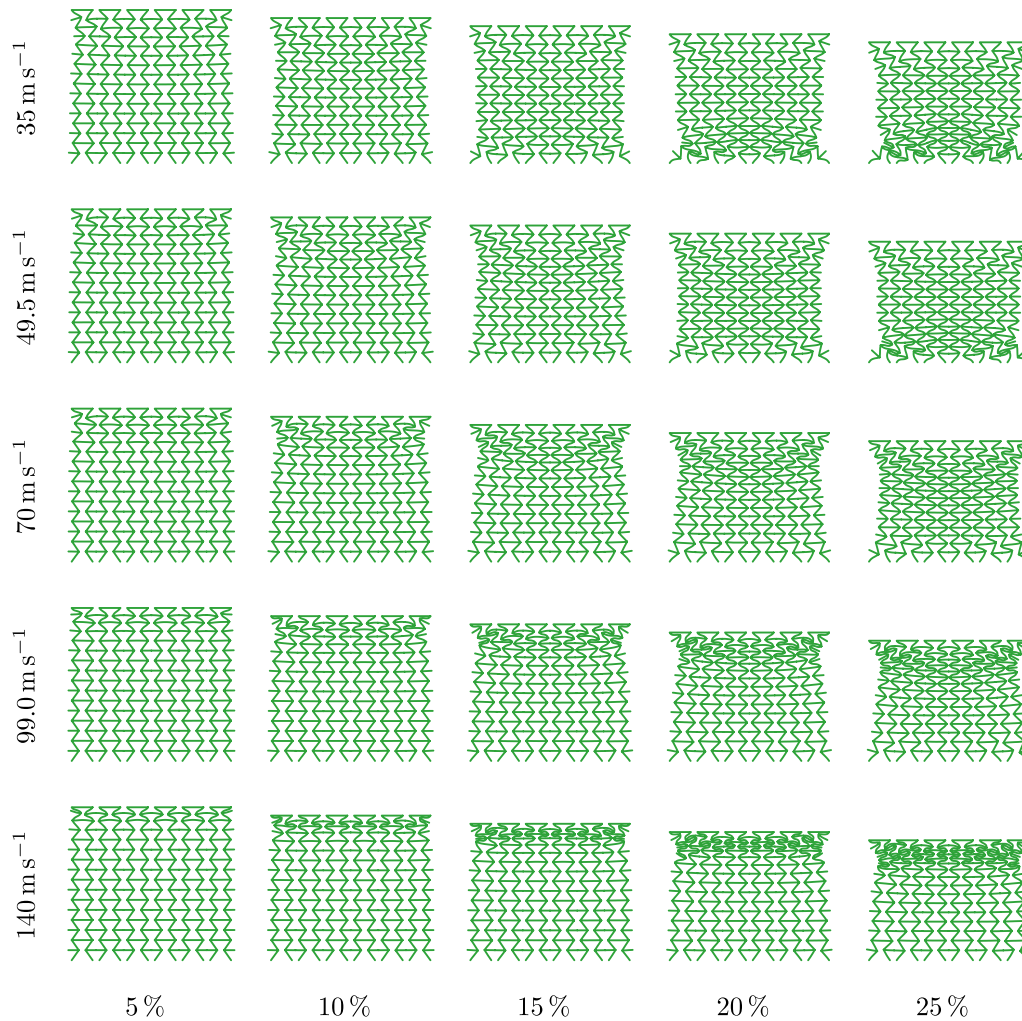
Fig. 4.11. Deformation patterns of the ARH sample of *Length 1* at different impact velocities and compression states.

Thus, it can be concluded that the impact mitigation efficacy of auxetic materials only appears in the case, where energy absorption and the need to limit the deformation of the protective structure at a given stiffness are the main measures. In other cases, especially when the spreading of the load or lightweight design of the protective structures are of interest, auxetic structures are not able to spread the load of a localized impact and perform worse than conventional honeycombs when considering equal mass even in pure energy absorption measures.

Lastly, investigations with different scenarios as well as size effects using faster, albeit less accurate, beam-based simulations were conducted to explore other patch configurations. In the first trial, the investigation into even longer samples lead to no significant difference between patches of *Length 2* and *Length 4*, emphasizing the assumption that the earlier investigations are representative of a local impact onto a wide structure. The contradiction with [9], where wider samples are suggested to be required for assessment of the performance of the structure, can be explained by the limitation to elasticity in that study, whereas plasticity, especially in this dynamic environment, can lead to higher localization, which prevents further spreading of the load. To this end as well, different unit cell sizes were compared in another investigation. Here no significant effect was observed, leading to the conclusion, that the investigated number of unit cells reported in Table 2.3 can be taken as sufficient to not experience significant boundary

effects. This is especially valuable when considering the physical tests, where smaller unit cells would require more refined manufacturing, that might be limited by technological or budgetary constraints.

This full-scale, physical testing campaign is needed to ensure all physical phenomena have been considered. Physical tests, especially when considering ballistic impact studies, require tremendous effort and resources to be conducted and have, as was demonstrated, difficulties to ensure the boundary conditions envisioned are met with certainty. To this end numerical tests enable faster and less resource-intensive assessment with properly idealized boundary conditions. In numerical investigations, the placement of sensors is not a matter of physical practicality, but rather of limiting the amount of data, enabling a better understanding of the inside processes in the material and the detailed interactions with the surrounding structure. As there are different levels of refinement and discretization of structures, one needs to make good use of all available resources in order to speed up the design and research process and to further facilitate the understanding and development of protection concepts.

Summarizing the findings of this contribution, the existing primer of literature, that auxetics perform better for impact mitigation, has been challenged by data of force distribution, where simple non-auxetic honeycombs were shown to exhibit better performance in multiple configurations. Also, the simple use of energy absorption as assessment
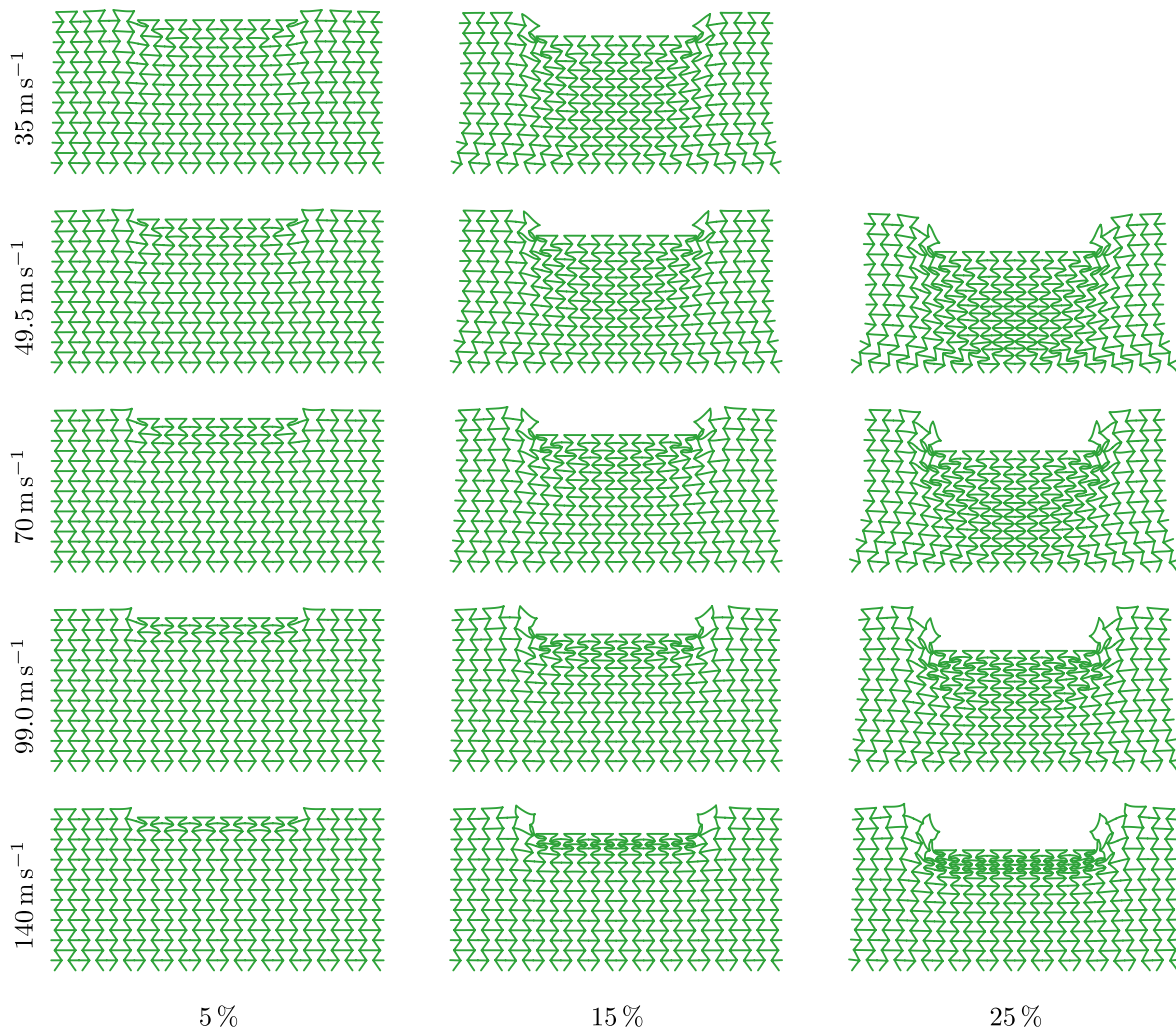
Fig. 4.12. Deformation patterns of the ARH sample of *Length 2* at different impact velocities and compression states.

tool for impact mitigation is insufficient in cases where not only the total energy absorbed by the structure is relevant for the safety of the protected structure, but also the distribution of the transmitted forces. To this end various numerical tools were shown to be effective supplements to the physical experiments in order to gain a deeper understanding, which can be used for the design of protective structures and further research on this topic. For this further research, the assessment of different auxetic and non-auxetic structures will be valuable for the community to ensure that findings can be generalized, as well as a deeper investigation into the interdependency of the inelastic, strain-rate dependent response and different unit cell architectures.

CRediT authorship contribution statement

**Til Gärtner:** Writing – original draft, Visualization, Validation, Software, Methodology, Investigation, Data curation, Conceptualization. **Richard Dekker:** Writing – review & editing, Software, Methodology, Investigation, Data curation, Conceptualization. **Dennis van Veen:** Writing – review & editing, Resources, Methodology, Investigation, Conceptualization. **Sanne J. van den Boom:** Writing – review & editing, Supervision, Project administration, Methodology, Investigation, Conceptualization. **Lucas Amaral:** Writing – review & editing, Validation, Project administration, Methodology, Investigation, Conceptualization.

Appendix A. Construction drawings
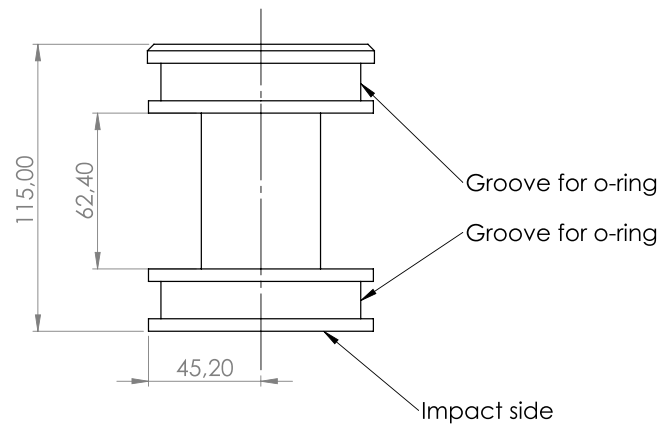
Fig. A.1. Plunger with main dimensions in mm.

Appendix B. Experimental and numerical comparisons
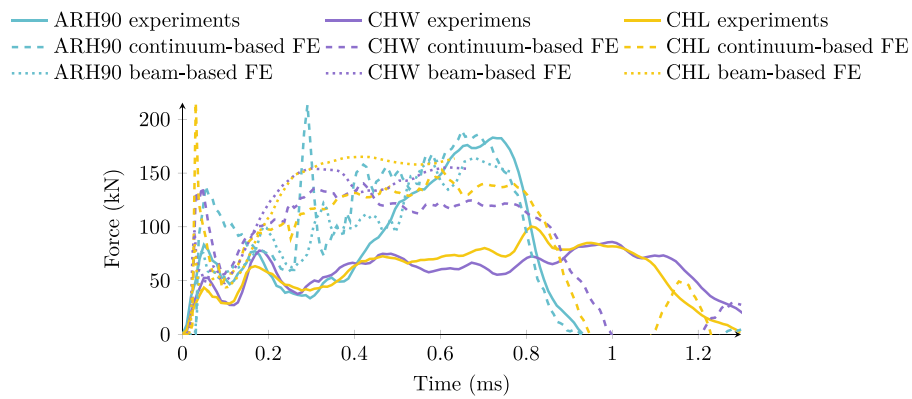
Fig. B.1. Comparison of experimental and numerical results for the SS configuration.
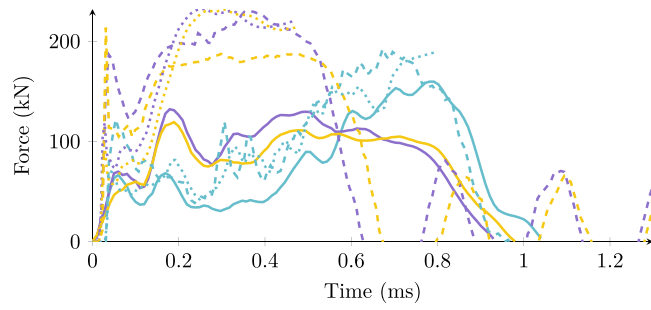
Fig. B.2. Comparison of experimental and numerical results for the SM configuration.

Appendix C. Structural samples comparisons

(a) *Length 1*

(b) *Length 2*
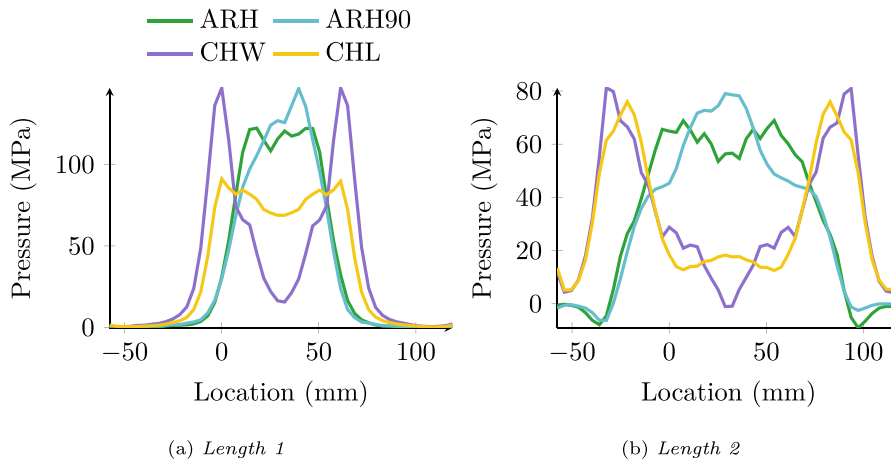
Fig. C.1. Comparison of the average pressure over the back-face for the SM configuration using the continuum-based model.
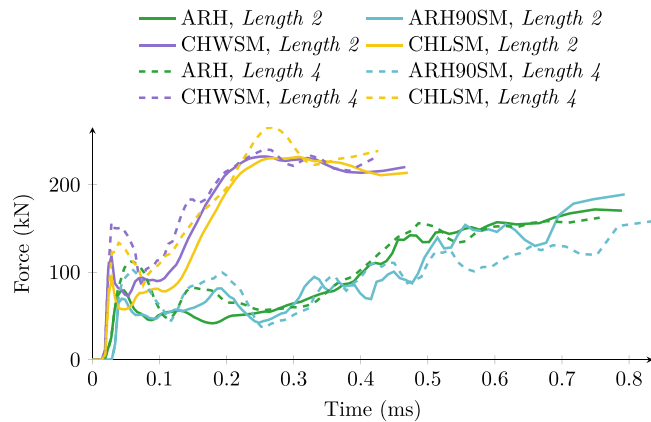
Fig. C.2. Comparison of wider samples for the SM configuration using the beam-based model.
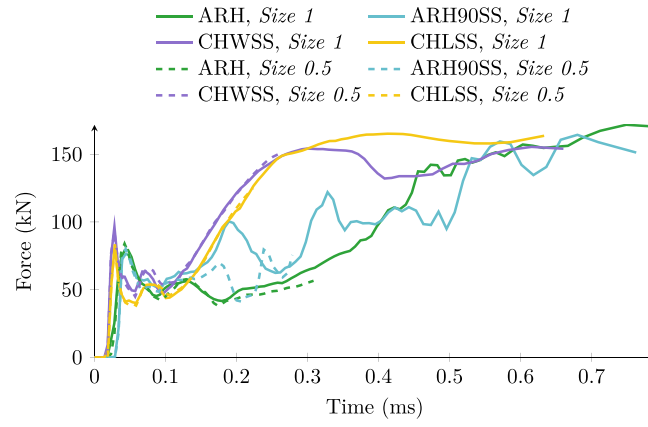
Fig. C.3. Comparison of smaller unit cells for the SS configuration of *Length 2* using the beam-based model.
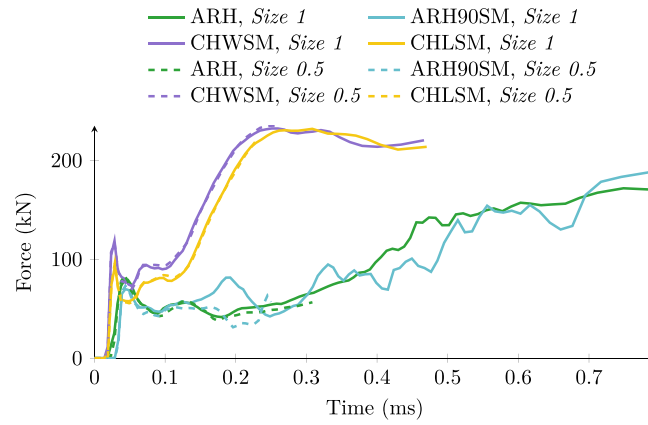
Fig. C.4. Comparison of smaller unit cells for the SM configuration using the beam-based model.
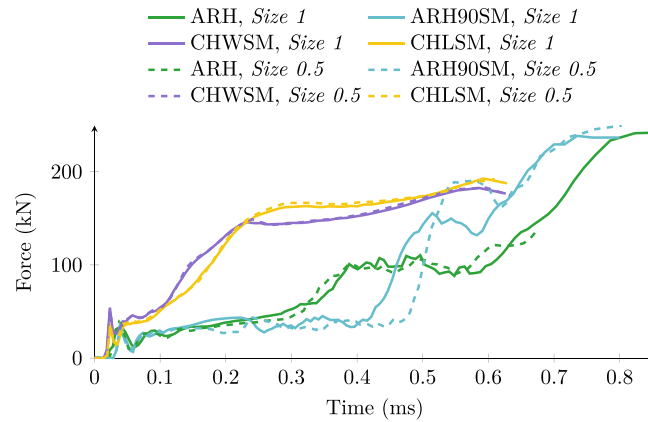
Fig. C.5. Comparison of smaller unit cells for the SM configuration *Length 1* using the beam-based model.

Appendix D. Deformation patterns at different speeds
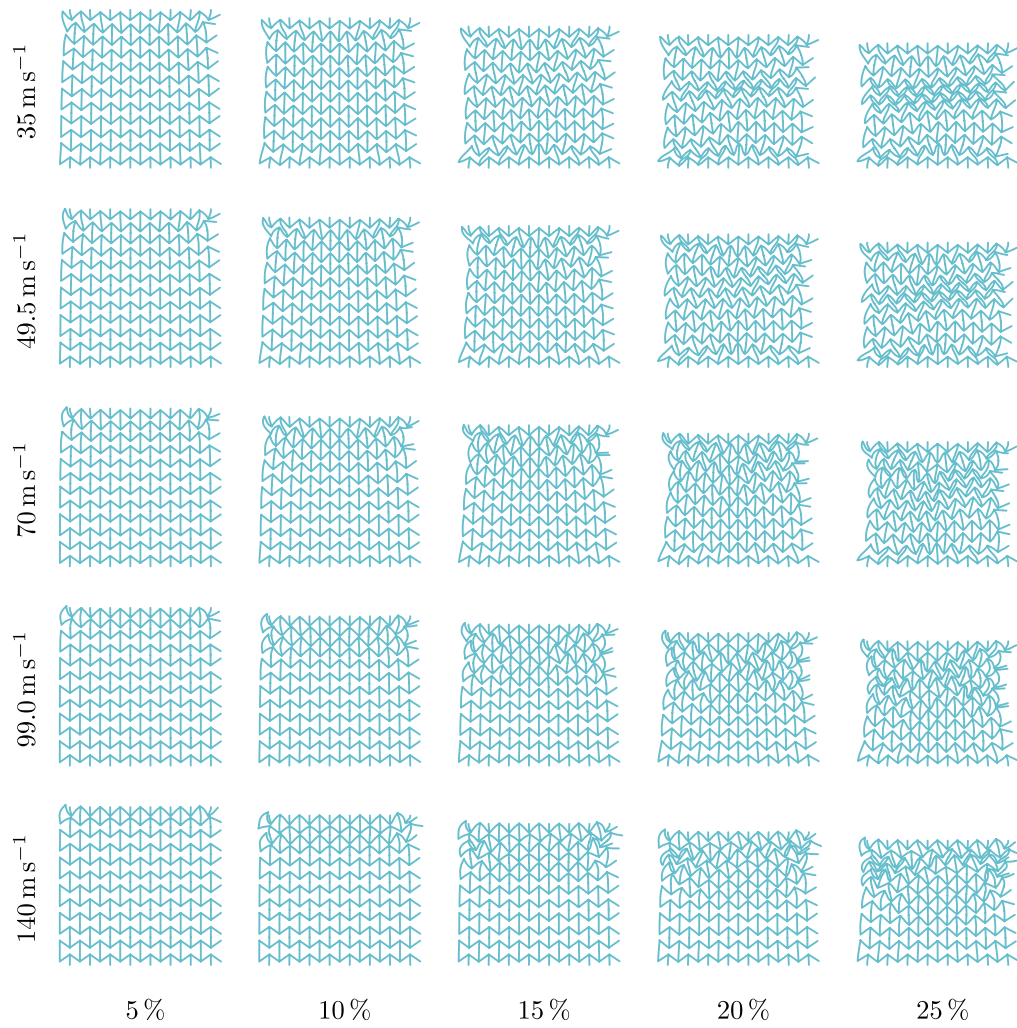
Fig. D.1. Deformation patterns of the ARH90SM sample of *Length 1* at different impact velocities and compression states.
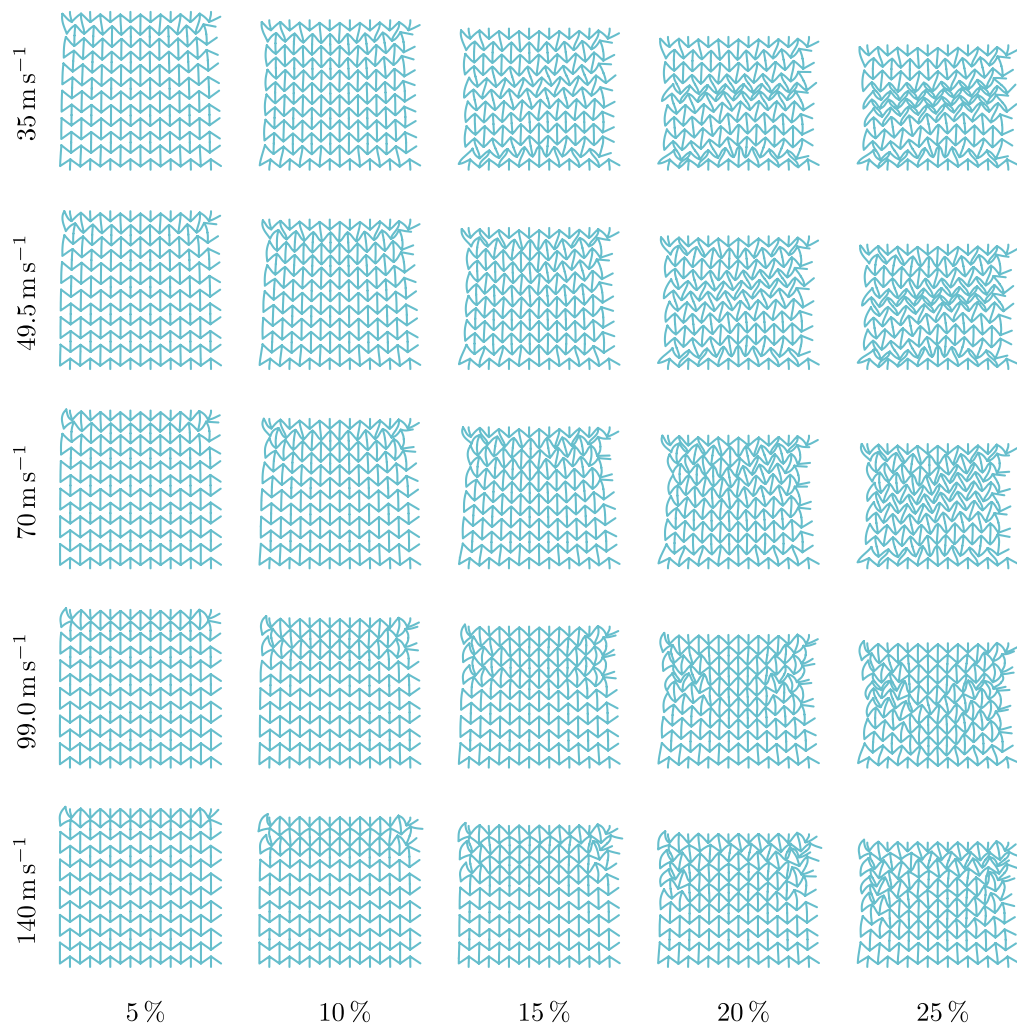
Fig. D.2. Deformation patterns of the ARH90SS sample of *Length 1* at different impact velocities and compression states.
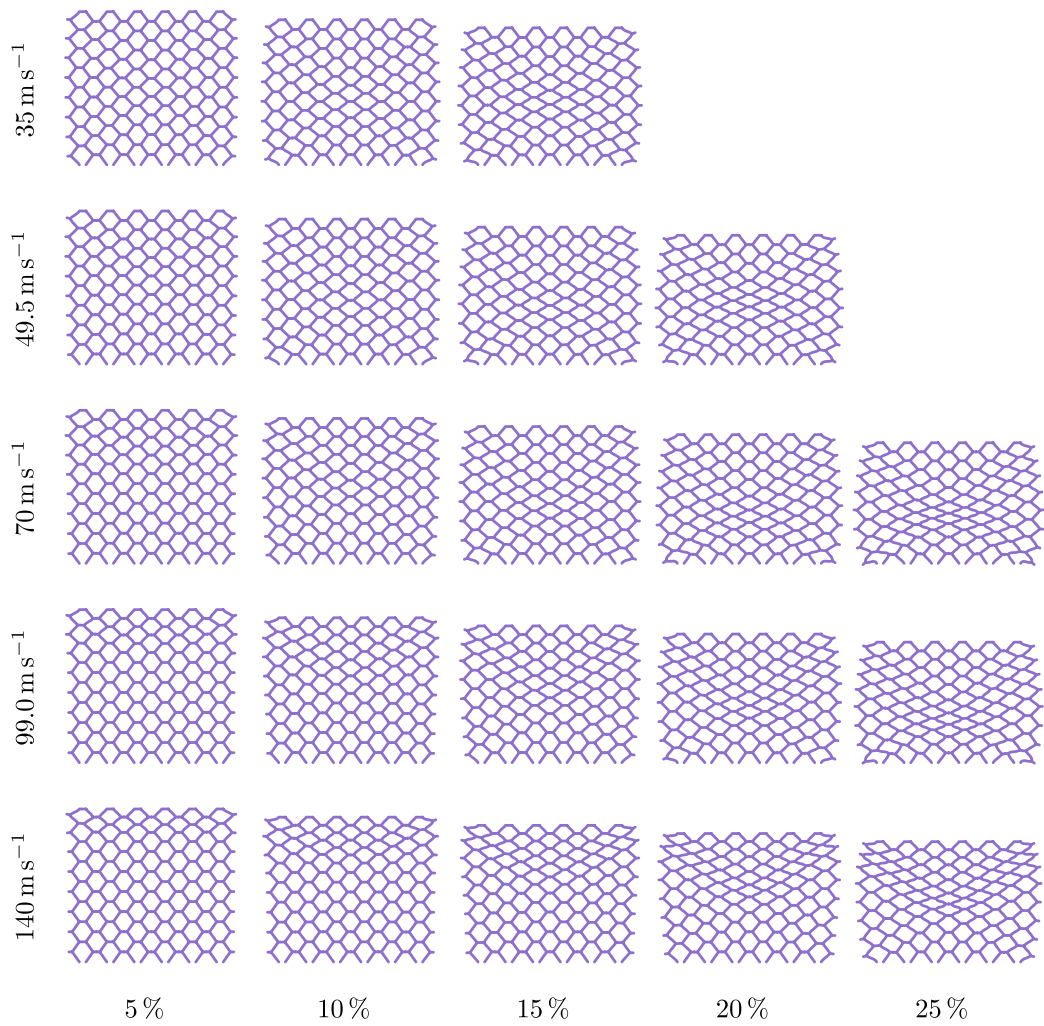
Fig. D.3. Deformation patterns of the CHWSM sample of *Length 1* at different impact velocities and compression states.
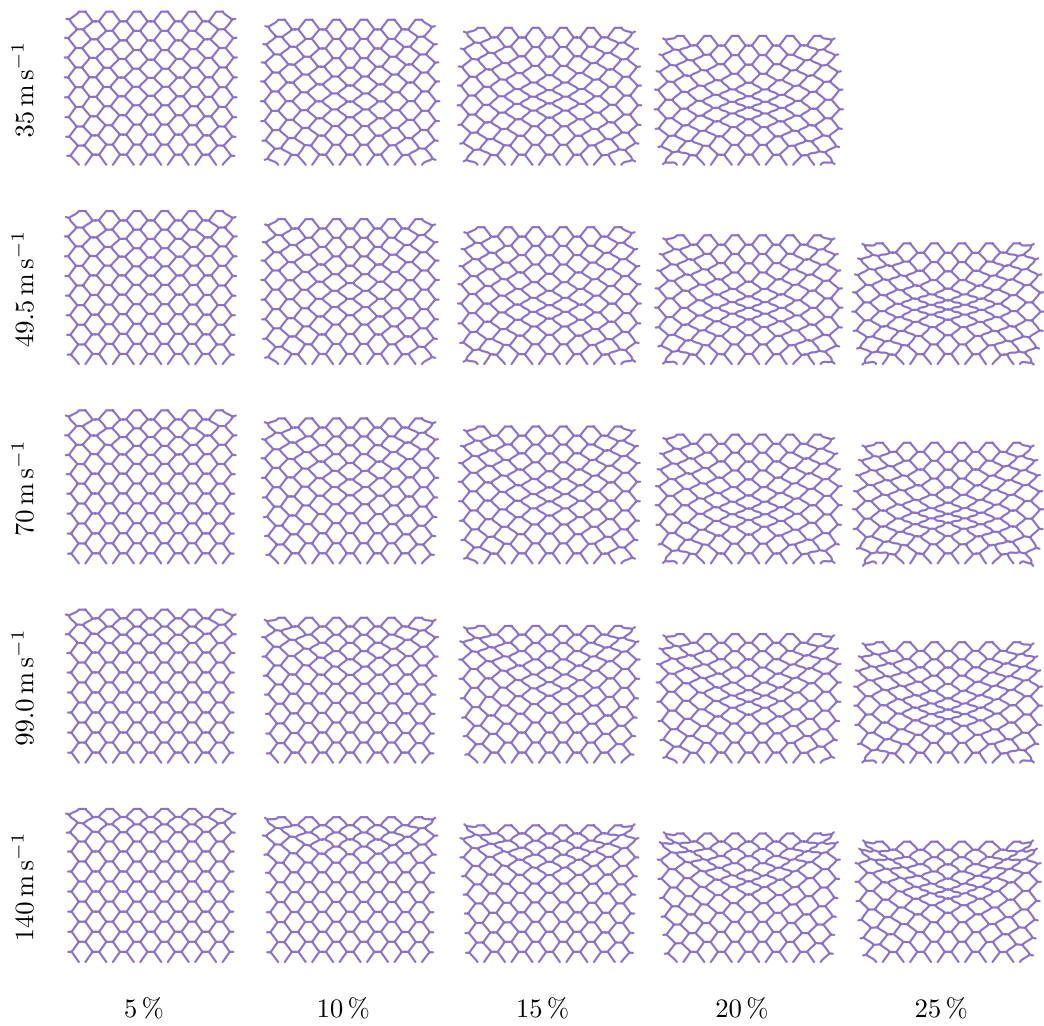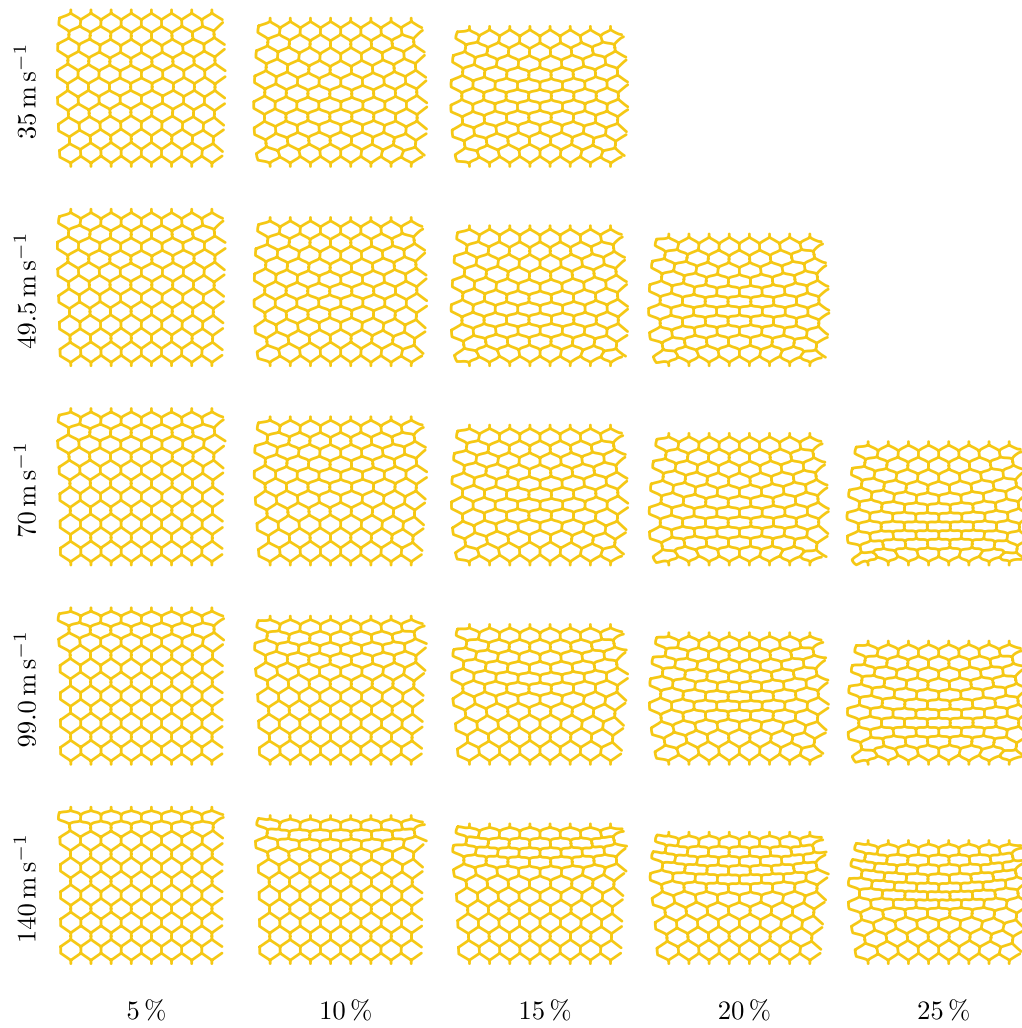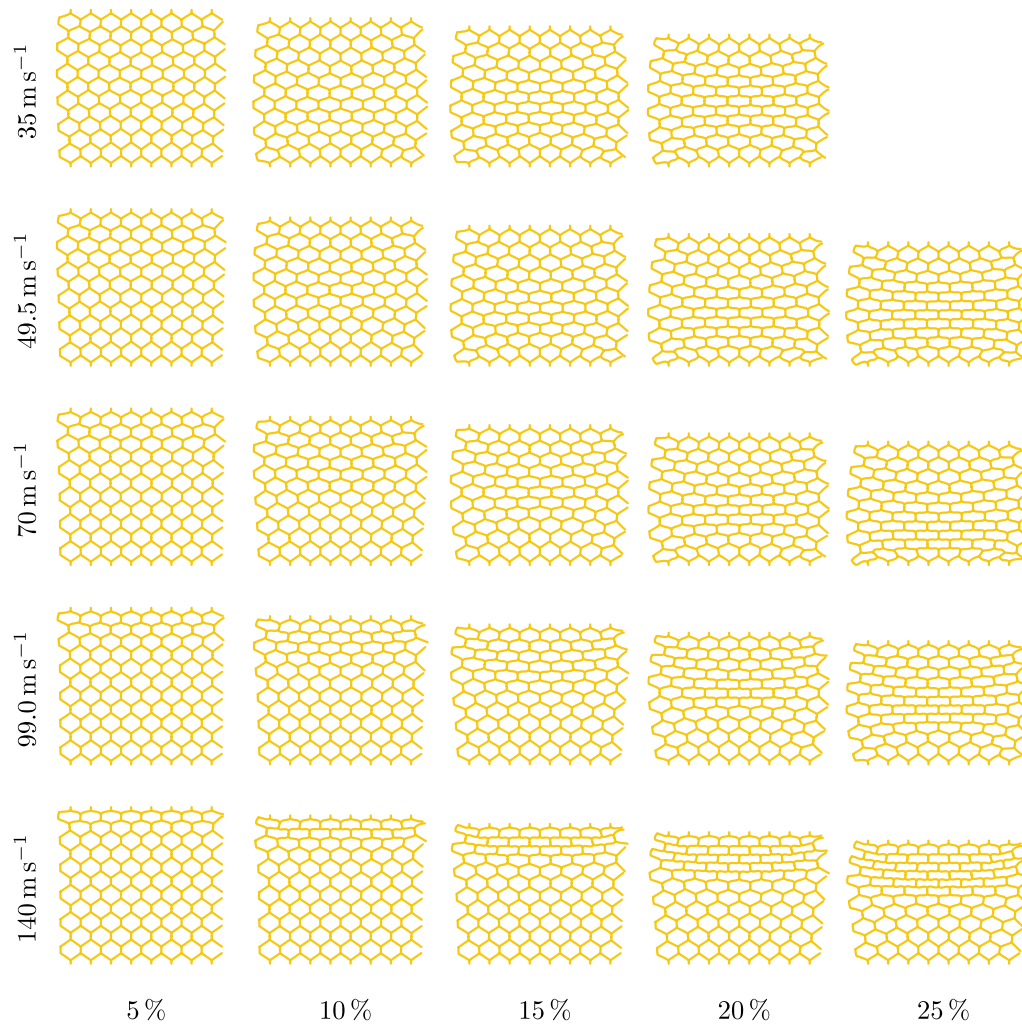
Fig. D.4. Deformation patterns of the CHWSS sample of *Length 1* at different impact velocities and compression states.
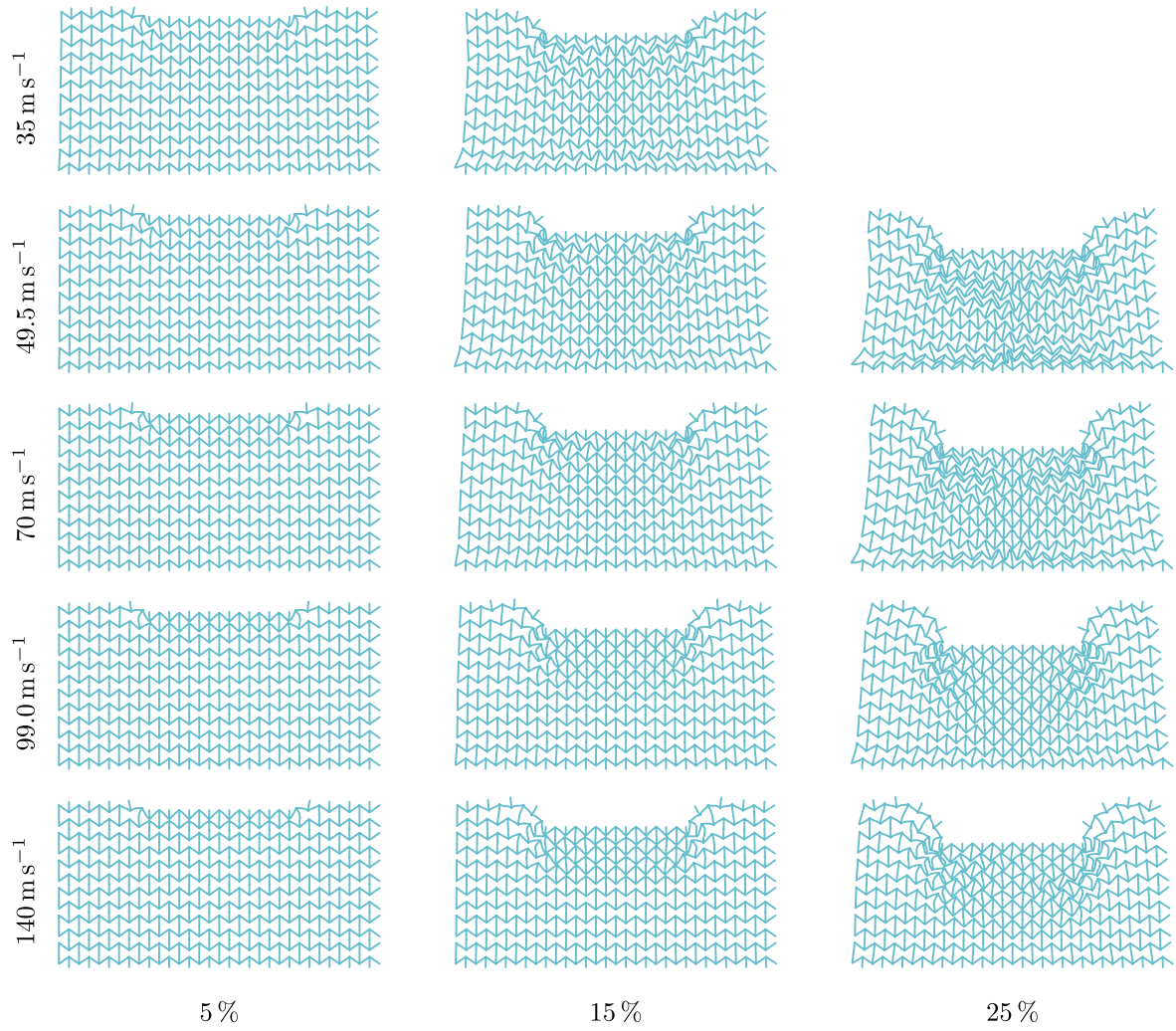
Fig. D.5. Deformation patterns of the CHLSM sample of *Length 1* at different impact velocities and compression states.

Fig. D.6. Deformation patterns of the CHLSS sample of *Length 1* at different impact velocities and compression states.

Fig. D.7. Deformation patterns of the ARH90SM sample of *Length 2* at different impact velocities and compression states.
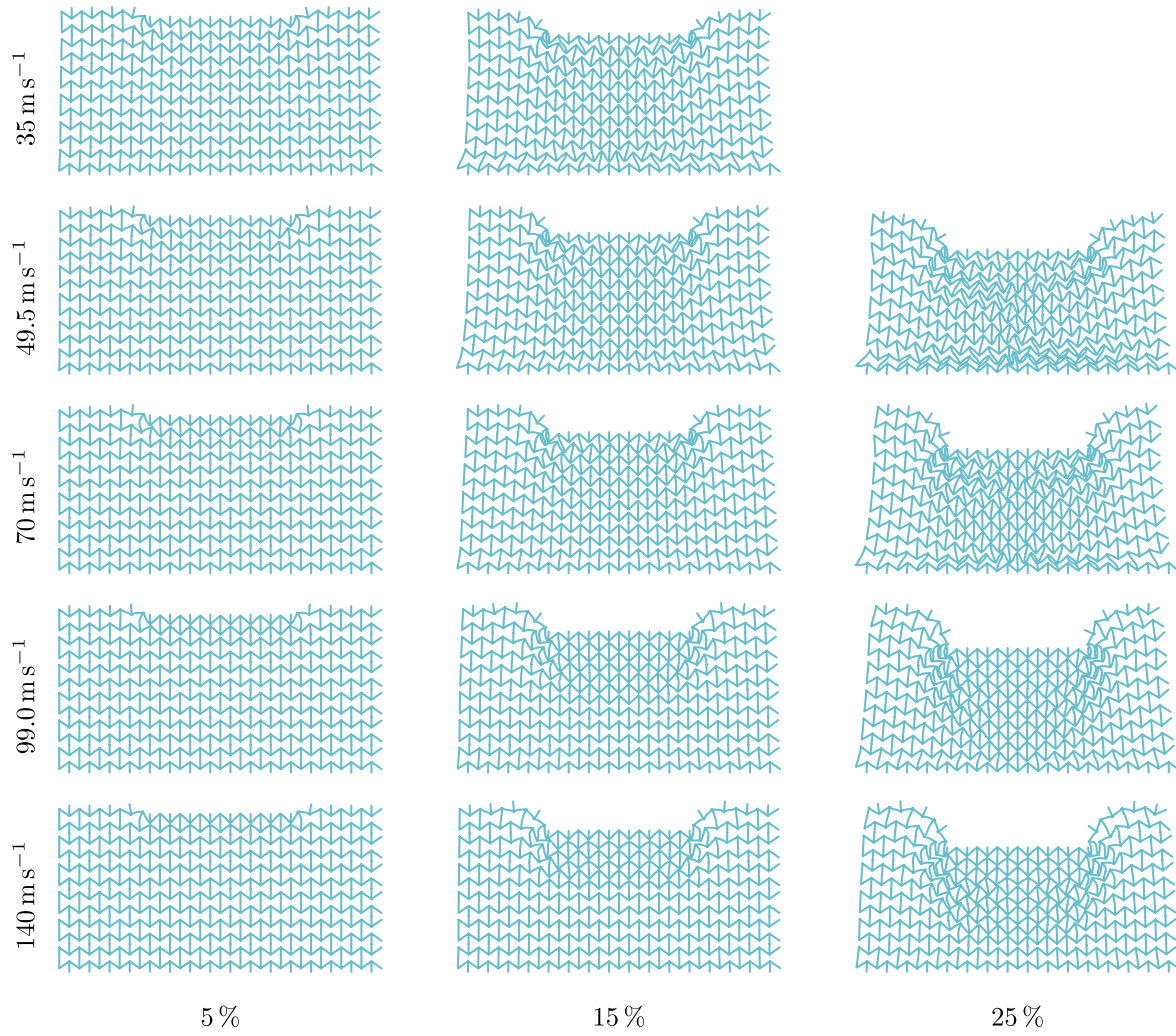
Fig. D.8. Deformation patterns of the ARH90SS sample of *Length 2* at different impact velocities and compression states.
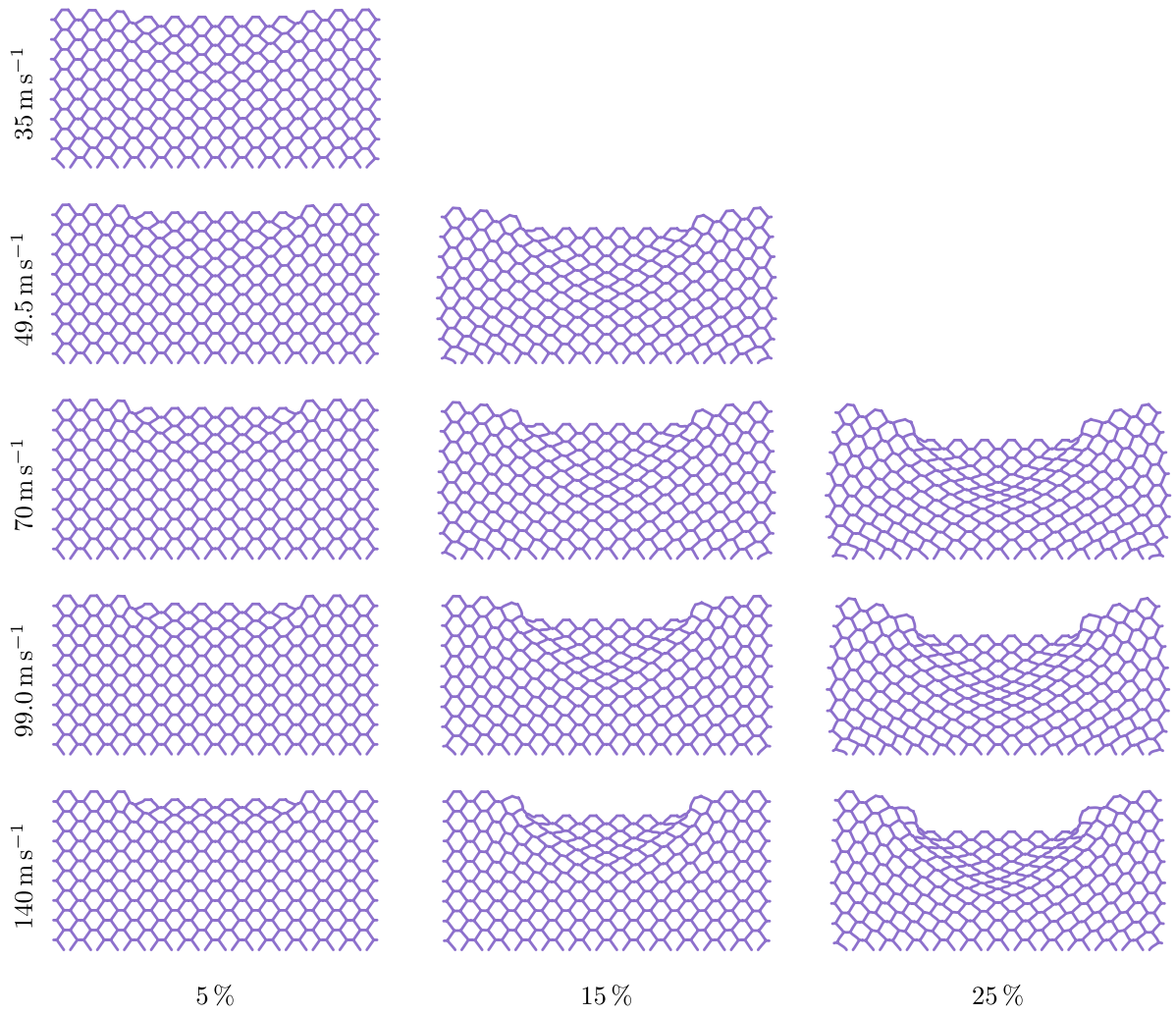
Fig. D.9. Deformation patterns of the CHWSM sample of *Length 2* at different impact velocities and compression states.
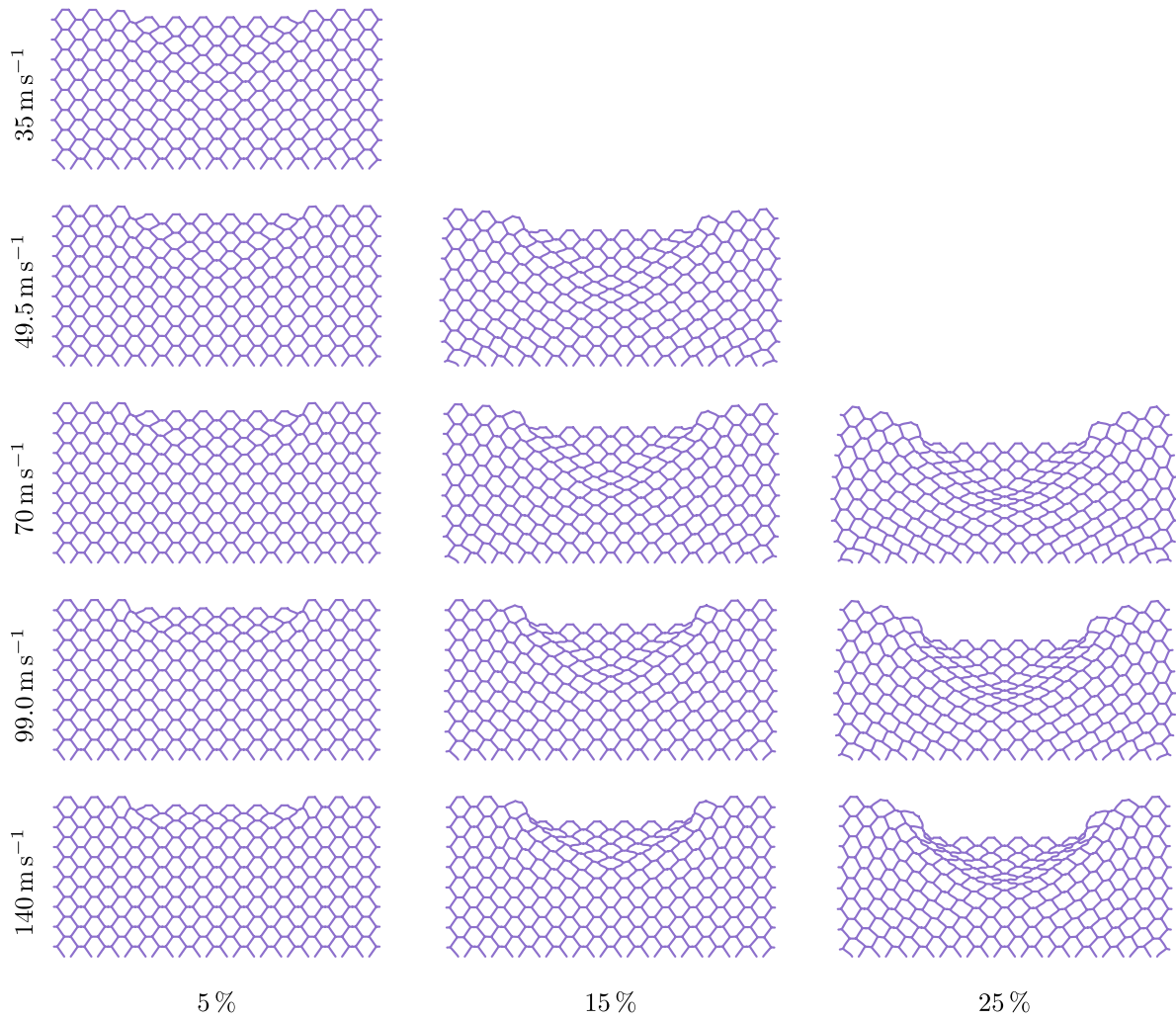
Fig. D.10. Deformation patterns of the CHWSS sample of *Length 2* at different impact velocities and compression states.
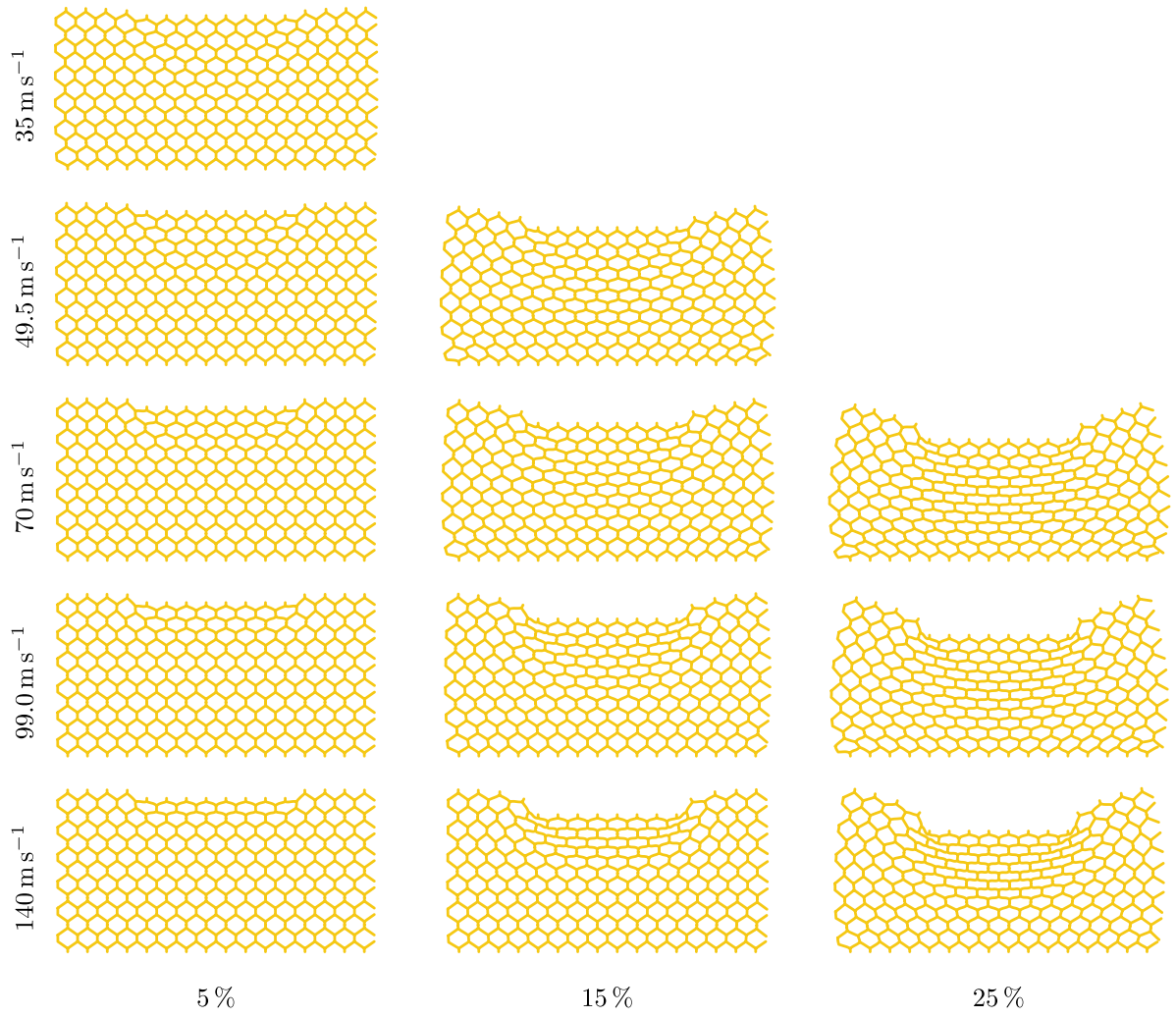
Fig. D.11. Deformation patterns of the CHLSM sample of *Length 2* at different impact velocities and compression states.
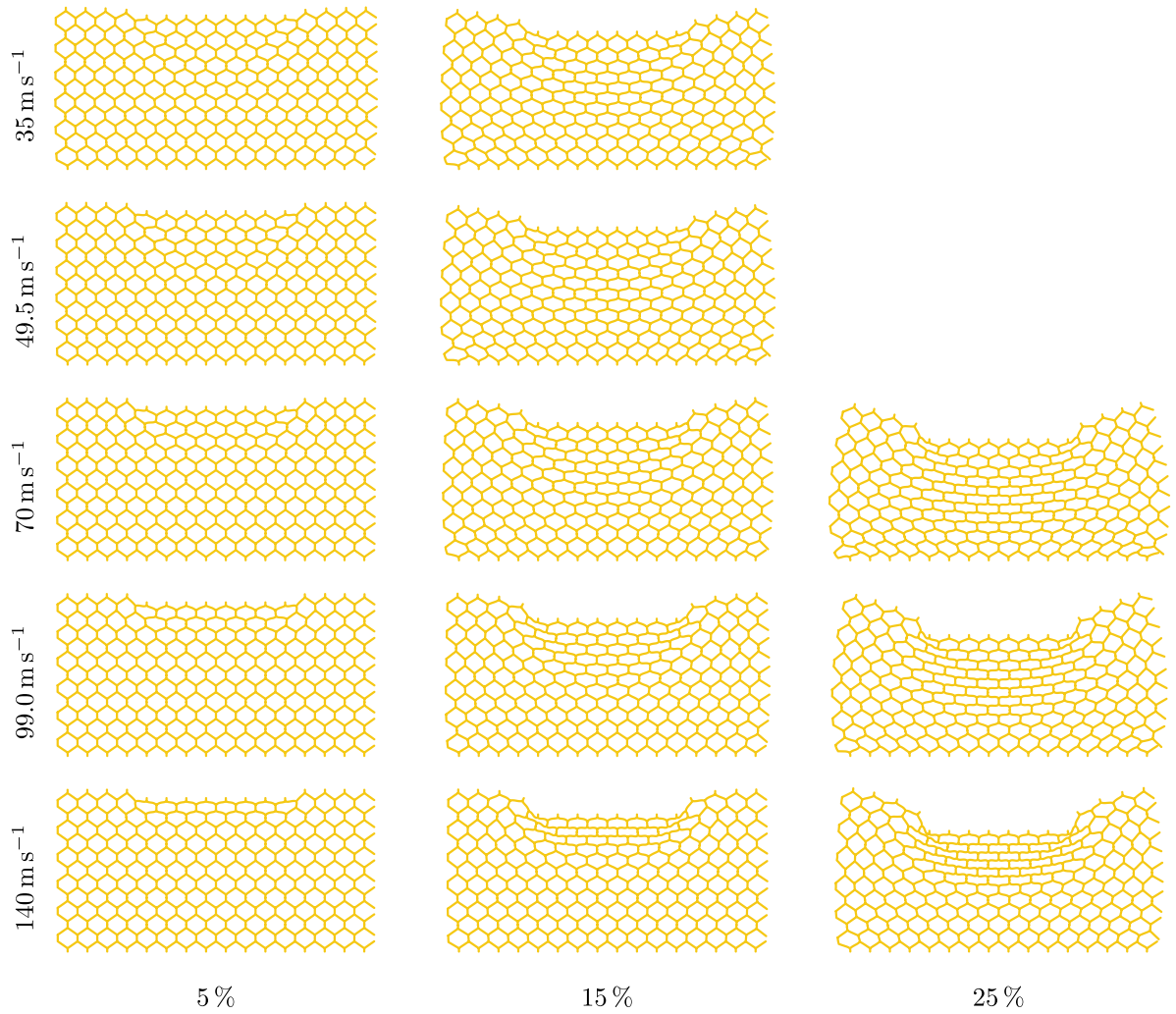
Fig. D.12. Deformation patterns of the CHLSS sample of *Length 2* at different impact velocities and compression states.

Data availability

Data will be made available on request.

References

[1] Fink BK. Performance metrics for composite integral armor. J Thermoplast Compos Mater 2000;13:417–31. http://dx.doi.org/10.1106/fr0l-t33w-jpd0-vfh3.

[2] Bohara RP, Linforth S, Nguyen T, Ghazlan A, Ngo T. Anti-blast and -impact performances of auxetic structures: A review of structures, materials, methods, and fabrications. Eng Struct 2023;276. http://dx.doi.org/10.1016/j.engstruct.2022.115377.

[3] Ren X, Das R, Tran P, Ngo TD, Xie YM. Auxetic metamaterials and structures: a review. Smart Mater Struct 2018;27. http://dx.doi.org/10.1088/1361-665X/aaa61c.

[4] Galea Mifsud R, Muscat GA, Grima-Cornish JN, Dudek KK, Cardona MA, Attard D, Farrugia PS, Gatt R, Evans KE, Grima JN. Auxetics and fea: Modern materials driven by modern simulation methods. Mater (Basel) 2024;17. http://dx.doi.org/10.3390/ma17071506, URL: https://www.ncbi.nlm.nih.gov/pubmed/38612021.

[5] Critchley R, Corni I, Wharton JA, Walsh FC, Wood RJK, Stokes KR, manufacture Areviewofthe. Mechanical properties and potential applications of auxetic foams. Phys Status Solidi (B) 2013;250:1963–82. http://dx.doi.org/10.1002/pssb.201248550.

[6] Saxena KK, Das R, Calius EP. Three decades of auxetics research – materials with negative Poisson's ratio: A review. Adv Eng Mater 2016;18:1847–70. http://dx.doi.org/10.1002/adem.201600053.

[7] Weeger O, Valizadeh I, Mistry Y, Bhate D. Inelastic finite deformation beam modeling, simulation, and validation of additively manufactured lattice structures. Addit Manuf Lett 2023;4. http://dx.doi.org/10.1016/j.addlet.2022.100111.

[8] Kappe K, Hoschke K, Riedel W, Hiermaier S. Multi-objective optimization of additive manufactured functionally graded lattice structures under impact. Int J Impact Eng 2023. http://dx.doi.org/10.1016/j.ijimpeng.2023.104789.

[9] Gärtner T, van den Boom SJ, Weerheijm J, Sluys LJ. Geometric effects on impact mitigation in architected auxetic metamaterials. Mech Mater 2024;191:104952. http://dx.doi.org/10.1016/j.mechmat.2024.104952.

[10] Bohara RP, Linforth S, Ghazlan A, Nguyen T, Remennikov A, Ngo T. Performance of an auxetic honeycomb-core sandwich panel under close-in and far-field detonations of high explosive. Compos Struct 2022;280. http://dx.doi.org/10.1016/j.compstruct.2021.114907.

[11] Qi C, Remennikov A, Pei L-Z, Yang S, Yu Z-H, Ngo TD. Impact and close-in blast response of auxetic honeycomb-cored sandwich panels: Experimental tests and numerical simulations. Compos Struct 2017;180:161–78. http://dx.doi.org/10.1016/j.compstruct.2017.08.020.

[12] Liu W, Wang N, Luo T, Lin Z. In-plane dynamic crushing of re-entrant auxetic cellular structure. Mater Des 2016;100:84–91. http://dx.doi.org/10.1016/j.matdes.2016.03.086.

[13] Gupta YM, Ding JL. Impact load spreading in layered materials and structures: concept and quantitative measure. Int J Impact Eng 2002;27:277–91. http://dx.doi.org/10.1016/s0734-743x(01)00051-3.

[14] Gibson LJ, Ashby MF, Schajer GS, Robertson CI. The mechanics of two-dimensional cellular materials. Proc R Soc A 1997;382:25–42. http://dx.doi.org/10.1098/rspa.1982.0087.

[15] Johnson GR, Cook WH. Fracture characteristics of three metals subjected to various strains, strain rates, temperatures and pressures. Eng Fract Mech 1985;21:31–48. http://dx.doi.org/10.1016/0013-7944(85)90052-9.

[16] Spradlin TJ. Process sequencing for fatigue life extension of large scale laser peened components (Dissertation), Wright State University; 2011, URL: https://corescholar.libraries.wright.edu/etd_all/495/.

[17] Umbrello D, M'Saoubi R, Outeiro JC. The influence of johnson-cook material constants on finite element simulation of machining of aisi 316l steel. Int J Mach Tools Manuf 2007;47:462–70. http://dx.doi.org/10.1016/j.ijmachtools.2006.06.006.

[18] Reissner E. On finite deformations of space-curved beams. ZAMP Z Angew Math Phys 1981;32:734–44. http://dx.doi.org/10.1007/bf00946983.

[19] Simo JC. A finite strain beam formulation, the three-dimensional dynamic problem. part i. Comput Methods Appl Mech Engrg 1985;49:55–70. http://dx.doi.org/10.1016/0045-7825(85)90050-7.

[20] Dynaflow Research Group. Jive. 2021, URL: https://dynaflow.com/software/jive/.

[21] Simo JC, Vu-Quoc L. A three-dimensional finite-strain rod model, part ii: Computational aspects. Comput Methods Appl Mech Engrg 1986;58:79–116. http://dx.doi.org/10.1016/0045-7825(86)90079-4.

[22] Crisfield MA, Jelenić G. Objectivity of strain measures in the geometrically exact three-dimensional beam theory and its finite-element implementation. Proc R Soc Lond Ser A Math Phys Eng Sci 1999;455:1125–47. http://dx.doi.org/10.1098/rspa.1999.0352.

[23] Gärtner T, van den Boom SJ, Weerheijm J, Sluys LJ. A strategy for scaling the hardening behavior in finite element modelling of geometrically exact beams. Comput Mech 2025;75:1471–82. http://dx.doi.org/10.1007/s00466-024-02572-3.

[24] Smriti A Kumar, Steinmann P. A finite element formulation for a direct approach to elastoplasticity in special cosserat rods. Internat J Numer Methods Engrg 2020. http://dx.doi.org/10.1002/nme.6566.

[25] Wriggers P, Simo JC. A note on tangent stiffness for fully nonlinear contact problems. Commun Appl Numer Methods 1985;1:199–203. http://dx.doi.org/10.1002/cnm.1630010503.

[26] Ruan D, Lu G, Wang B, Yu TX. In-plane dynamic crushing of honeycombs—a finite element study. Int J Impact Eng 2003;28:161–82. http://dx.doi.org/10.1016/s0734-743x(02)00056-8.